Supporting Information

Polymerization-Like Co-Assembly of Silver Nanoplates and Patchy Spheres

Binbin Luo,[†] John W. Smith,[†] Zixuan Wu,[†] Juyeong Kim,[†,‡] Zihao Ou,[†] Qian Chen[†,‡,§]*

[†]Department of Materials Science and Engineering, [‡]Frederick Seitz Materials Research Laboratory, and [§]Department of Chemistry, University of Illinois at Urbana-Champaign, Urbana, Illinois 61801, United States

*To whom correspondence should be addressed. Email: qchen20@illinois.edu

Materials and Methods

Chemicals

Sodium citrate tribasic dihydrate (≥99.0%, $HOC(COONa)(CH_2COONa)_2 \cdot 2H_2O$, Sigma-Aldrich), sodium borohydride (99%, $NaBH_4$, Sigma-Aldrich), silver nitrate (≥99.0%, $AgNO_3$, Sigma-Aldrich), L-Ascorbic acid (BioXtra, ≥ 99.0%, Sigma-Aldrich), sodium thiosulfate (≥98.0%, $Na_2S_2O_3$, Sigma-Aldrich), potassium hexacyanoferrate(II) trihydrate (98.5 − 102.0%, $K_4Fe^{II}(CN)_6 \cdot 3H_2O$, Sigma-Aldrich), potassium hexacyanoferrate(III) (≥99.0%, $K_3Fe^{III}(CN)_6$, Sigma-Aldrich), sodium dodecyl sulfate (≥99.0%, SDS, Sigma-Aldrich), potassium hydroxide (≥85.0%, KOH, Fisher Scientific), citric acid monohydrate (99.0−102.0%, $(HO_2CCH_2)_2$-$C(OH)(CO_2H) \cdot H_2O$, Fisher Scientific), sodium chloride (99.3%, NaCl, Fisher Scientific), hydrogen peroxide (30 wt %, H_2O_2, Macron), and 2-(2-[2-(11-mercapto-undecyloxy)-ethoxy]-ethoxy)-ethoxy-ethoxy-ethoxy-acetic acid (≥95%, $HS(CH_2)_{11}(OC_2H_4)_6OCH_2COOH$, Prochimia Surfaces) were purchased and used without further purification. All glassware was treated with aqua regia (a mixture of HCl and HNO_3 with a volume ratio of 3:1), thoroughly rinsed with water, and dried immediately before use. Nanopure water (18.2 MΩ·cm at 25 °C) purified by a Milli-Q Advantage A10 system was used for all washing and solution preparation.

Synthesis of anisometric silver nanoplates

A modified seeded-growth method was used to synthesize anisometric silver nanoplates.[1] Silver seeds were prepared first, by sequential addition of aqueous solutions of $AgNO_3$ (25 mL, 0.1 mM), sodium citrate (600 μL, 75 mM), and hydrogen peroxide (30 wt %, 60 μL) to a 125 mL Erlenmeyer flask being stirred at 300 rpm at room temperature in air. After addition of the hydrogen peroxide, the stirring speed was increased to 1050 rpm before rapid injection of a freshly prepared aqueous $NaBH_4$ solution (250 μL, 0.1 M). This $NaBH_4$ solution was prepared by adding water which had been precooled in an ice bath for 10 min to solid $NaBH_4$ and vortexing immediately. The seed solution turned blue approximately 4−10 min after the injection of the $NaBH_4$ solution and was kept stirring for another 5 min after this color change. Then the seed solution was centrifuged (using an Eppendorf Centrifuge 5804) at 10500 rpm for 8 min and the sediment was redispersed in 10 mL 0.94 mM sodium citrate solution. A UV−vis spectrum of the as-prepared seeds was measured using a Scinco S-4100 PDA spectrophotometer. From batch to batch, the extinction peak position was at wavelengths between 700 and 800 nm (Figure S1A). In a typical seeded-growth process, the seed solution was diluted until a peak intensity value of 0.012 was achieved, using additional 0.94 mM sodium citrate solution. Then, 0.75 mL L-Ascorbic acid (0.1 M) was added to 20 mL of this diluted seed solution in a 40 mL glass vial (Fisherbrand, 29 mm × 94 mm).

A separate solution was prepared by mixing 20 mL $AgNO_3$ (1.0 mM), 0.125 mL citric acid (0.1 M), and 0.1 mL sodium citrate (1.5 mM). This solution was added to the seed solution dropwise through a syringe

pump (Fusion 200, Chemyx Inc.) with an injection rate of 0.4 mL/min. After 5 min (2 mL) of injection, two-thirds of the reaction solution was removed, and the remaining amount was used as a source of seeds for the next growth cycle. The removed products of the first few cycles were discarded (since the nanoplates at these stages were still small) but samples from cycles 3, 4, and 5 were collected in separate 8 mL glass vials (Wheaton). During the whole growth process, the seed solution was shaking vigorously at room temperature with a thermomixer (Eppendorf, ThermoMixer C) at a shaking speed of 300−1000 rpm. Silver nanoplates of different edge lengths were obtained from the products of different cycles (Figure S2). We found that the UV−vis extinction peak position measured from a solution of the prepared seeds, the injection rate, and the shaking speed during growth would also affect (or were related to) the edge length of the nanoplates. More details on the effects of these parameters are given in Table S1.

Thiol modification of silver nanoplates

The surfaces of silver nanoplates as-synthesized were coated with citrate ligands. These ligands were exchanged with carboxylate−thiol molecules ($HS(CH_2)_{11}(OC_2H_4)_6OCH_2COOH$) to improve colloidal stability in solution. This exchange was performed, first, by adding 200 μL of a 7.93 mM thiol ligand solution to 2 mL of a silver nanoplate sample solution directly collected from a certain growth cycle. This 7.93 mM thiol solution was prepared by adding 5 μL of the thiol as received from Prochimia to 1 mL water and vortexing immediately. After allowing the nanoplates to sit and sediment overnight and removing the resulting supernatant, 2 mL water was added to the sediment to dilute any free thiol ligands and residual ions. After 5 h of additional sedimentation, the supernatant of this solution was removed and the final product was stored in 1.5 mL water in an 8 mL glass vial (Wheaton).

Janus particle preparation

Janus particles were prepared by directional electron beam (e-beam) evaporation of gold onto a monolayer of colloidal polystyrene particles on a glass substrate.[2] A 2 wt % aqueous suspension (35 μL) of carboxylate−polystyrene particles (F8825, Invitrogen, 2 μm in diameter) was spread on a glass slide (7.6 cm × 2.5 cm) which had been pretreated with Piranha solution (a mixture of H_2SO_4 and 30 wt % H_2O_2 with a volume ratio of 3:1) for 40 min. The particles were then dried with N_2 to form a sub-monolayer on the glass slide. Then, a 2 nm titanium coating (at a deposition rate of 0.3−0.4 Å/s), followed by a 15 nm gold coating (at a deposition rate of 1.0 Å/s), was deposited vertically on the monolayer using an electron beam evaporation system (Temescal). Next, the glass slide was sonicated (using a Fisher Scientific FS30H ultrasonic water bath) in 15 mL water in a 50 mL centrifuge tube for 40 s to detach the Janus particles from the glass slide. Then, the glass slide was removed from the solution and further sonication of this solution for at least 6 min was applied to break up any Janus particles linked by the gold coating and to obtain

dispersed Janus particles. After sedimentation for 3 h, most of the supernatant was removed, such that the volume of the remaining solution was 2 mL. This concentrated stock suspension was used for later characterization (Figure S9) and self-assembly experiments. Right before optical microscopy imaging, the Janus particle stock solution was sonicated for 6 min to break up any possible aggregations in the solution.

Triblock particle preparation

Triblock particles were prepared following a procedure from literature.[3] First, an 8 wt % suspension (in 80 μL water/ethanol with volume ratio of 1:1) of carboxylate−polystyrene particles (F8825, Invitrogen, 2 μm in diameter) was dropped onto a 1 cm × 1 cm Si wafer just barely covered by water in a petri dish. This Si wafer had been pretreated with Piranha solution (see above) to make its surface hydrophilic. The particle suspension quickly spread on the water surface and formed a monolayer covering nearly the entire air−water interface. Then, additional water was carefully added beneath the monolayer to lift the monolayer away from the particles in bulk water. Next, 10 μL of a 2 wt % SDS solution was added to condense the monolayer. After 3 h, the monolayer was picked up using a larger Si wafer (1.5 cm × 2.5 cm, also pretreated with Piranha solution) and dried in air. Next, a 2 nm titanium coating, followed by 25 nm gold coating, was deposited vertically on the particle monolayer (which had been picked up by the Si wafer) using the same electron beam deposition conditions as for Janus particles. After deposition, particles were lifted from the substrate with a polydimethylsiloxane (PDMS) stamp. The PDMS stamp was prepared by mixing Sylgard 184 agents (Dow Corning) with monomer and cross-linking agent at a weight ratio of 10:1 and curing this mixture in an oven at 70 °C and under vacuum conditions overnight. Before stamping, the surface of the PDMS was treated with oxygen plasma (Harrick Plasma Cleaner PDC-32G) at 150 mTorr pressure and low power (6.8 W) for 50 s. The particles inverted on the stamp then underwent a second titanium and gold deposition using the same conditions as the first deposition. After the second deposition, particles on the stamp were immersed in 20 mL gold etching solution for 80 s and then washed with 200 mL water three times. The etching solution was prepared by adding 4.93 g $Na_2S_2O_3$, 0.0994 g $K_4Fe^{II}(CN)_6 \cdot 3H_2O$, 0.667 g $K_3Fe^{III}(CN)_6$, and 11.2 g KOH to 200 mL water. Finally, the stamp was sonicated (Fisher Scientific, FS30H) in 15 mL water in a 50 mL centrifuge tube for 1 min to collect the triblock particles from the stamp. Then the stamp was removed from the solution and further sonication of this solution for at least 6 min was applied to obtain dispersed triblock particles. After sedimentation for 3 h, most of the supernatant was removed, such that the volume of the remaining solution was 1 mL. This concentrated stock suspension (Figure S18) was used for later experiments. Right before optical microscopy imaging, the triblock particle stock solution was sonicated for 6 min to break up any possible aggregations in the solution.

Sample characterization

The morphology of silver nanoplates was characterized using a Hitachi S4800 High-Resolution scanning electron microscope (SEM) and a JEOL 2100 Cryo transmission electron microscope (TEM). The thickness of carboxylate−thiol-coated silver nanoplates was measured using both tapping-mode atomic force microscopy (AFM, Asylum Research Cypher) and SEM when the nanoplates were in a standing configuration (Figure S1). The silicon wafer used in the AFM measurement was first washed with acetone and isopropanol, with sonication for 15 min in each solvent (Fisher Scientific, FS30H), and then treated with oxygen plasma (Harrick Plasma Cleaner PDC-23G) at medium power for 1 min to make the surface hydrophilic. Then, one drop of the silver nanoplate sample solution was put on the Si wafer and allowed to dry under ambient conditions. The zeta potential of carboxylate−thiol-coated silver nanoplates in pure water was measured using a Zetasizer Nano (Malvern) as -41.9 ± 6.8 mV.

Optical microscopy imaging

The particle suspension (~150 μL) was added to an 8-well chamber (composed of a 0.13 to 0.17 mm thick cover slip with plastic walls to make eight 0.2 to 0.4 mL wells, Chambered Coverglass, Thermo Scientific) for optical microscopy imaging. Bright-field optical microscopy imaging was performed using a Zeiss inverted microscope (Axiovert 200) with a 10× air objective (NA = 0.25), a 63× air objective (NA = 0.75) with 1.6× post-magnification, and 100× oil objectives (NA = 1.45 and 1.30). Optical microscopy movies were recorded using a complementary metal−oxide−semiconductor (CMOS) camera (Edmund Optics 5012 M GigE) at a rate of 17.21 to 20 frames per second (fps). Epifluorescence imaging was performed using a Zeiss inverted microscope (Observer.Z1) with a 100× oil objective (NA = 1.30) and an iXon electron-multiplying charge-coupled device (EMCCD) camera at a rate of 20 fps. A 532 nm laser line was used to excite fluorescence in Nile red fluorophores contained in the polystyrene particles. The particle suspension used for fluorescence microscopy imaging was prepared by first adding the well-mixed silver nanoplate and Janus particle solution (~150 μL) to the same type of 8-well chamber used for bright-field optical microscopy imaging. Typically, we used a Janus particle−nanoplate concentration ratio of 1:100. During imaging, sometimes both fluorescence microscopy and bright-field optical microscopy imaging were applied together in order to see both the fluorescent polystyrene particles and the non-fluorescent silver nanoplates. For all the chain length measurements from optical microscopy images or movies, we assigned a 5% error based on the resolution of the optical microscope. For the images and movies used in the main text and Supporting Information, we slightly adjusted the contrast and brightness in ImageJ or MATLAB, without changing any feature inside the images and movies.

Small-angle X-ray scattering (SAXS) measurements

SAXS measurements were performed on the chains assembled from silver nanoplates to determine the equilibrium center-to-center spacing between neighboring nanoplates in the chain. Measurements were made on chain solutions with two different ionic strengths, 1.4 and 3.0 mM. In each case, 100 μL of a concentrated chain sample at the desired ionic strength condition was gently transferred into a quartz capillary (1.5 mm outer diameter, 0.01 mm wall thickness, Hampton Research), which was then carefully sealed with poly(tetrafluoroethylene) (PTFE) tape to prevent evaporation. We then waited for 1 h for the sample to equilibrate. Right before the SAXS measurement, the capillary was gently inverted a few times to disperse the concentrated chains uniformly at the bottom of the capillary. Transmission SAXS spectra were collected for 30 min using a home-built setup (Forvis Technologies, Santa Barbara) with a Xenocs GeniX3D Cu Kα ultralow divergence X-ray source (1.54 Å/8 keV) with a divergence of ~1.3 mrad and a Pilatus 300 K 20 Hz hybrid pixel detector (Dectris). FIT2D (software from the European Synchrotron Radiation facility, http://www.esrf.eu/computing/scientific/FIT2D) was used to integrate 2D scattering plots and determine the intensity (I) and scattering vector (q) relation. SAXS spectra show a series of peaks in the detected q range (Figure 2B and Table S2). The fact that q values are integer multiples indicates a 1D lamellar structure.[4] Due to the large lattice spacing of the assembled chains, the first- or even second-order peaks (those with q values less than about 0.01 $Å^{-1}$) were overwhelmed by the profile of the unscattered beam. Consequently, the q values of these peaks were derived from higher-order peaks (Table S2). The d spacing, *i.e.*, the equilibrium center-to-center spacing between neighboring nanoplates in the chain, was calculated based on the derived first-order peak position (q_1) as $d = \frac{2\pi}{q_1}$.

Analysis and Calculations

Calculation of the percentage of deprotonated thiols at different pH conditions

The percentage of deprotonated carboxylate−thiol ligands on the silver nanoplate surfaces at equilibrium was calculated for different pH conditions using the Henderson−Hasselbalch equation: $\mathrm{pH} = \mathrm{p}K_\mathrm{a} + \log(\frac{[\mathrm{A}^-]}{[\mathrm{HA}]})$, where here $[\mathrm{A}^-]$ and $[\mathrm{HA}]$ are the molar concentrations of $–COO^-$ and –COOH groups, respectively, on the nanoplate surface. The $\mathrm{p}K_\mathrm{a}$ of the carboxylate−thiol ligands is between 3.5 and 3.7 (according to the manufacturer), and 3.5 was used for calculations here. Figure S3 shows the percentage of deprotonated carboxylate−thiol ligands on the nanoplate surface for various pH conditions. Based on the equation, over 99% of the carboxylate−thiol ligands are deprotonated at a pH higher than 5.5, leading to a strong electrostatic repulsion between nanoplates that prevents aggregation.

Calculation of the rate constant for face-to-face assembly of silver nanoplates (Figure 2C)

The assembly rate constant k for the face-to-face assembly of bifunctional silver nanoplates into 1D chains was calculated based on a model for the externally catalyzed polymerization of bifunctional monomers with identical functional groups.[5-7] This model follows $\bar{X}_n = 4[M]_0 kt + 1$, where $\bar{X}_n$ is the number-average degree of polymerization ($\bar{X}_n = \frac{\sum n_i i}{\sum n_i}$, where n_i is the number of chains containing i nanoplates), $[M]_0$ is the initial molar concentration of silver nanoplates in the field of view, and t is the reaction time. For the data presented in Figure 2C, we used the combined length of all the chains in the viewing area, L_{tot} (on average at different times, 110.9 μm (Figure S5B)), and the center-to-center spacing between neighboring nanoplates in the chain, d (116.6 nm, from SAXS measurement at this ionic strength condition), to estimate the total number of silver nanoplates in the field of view as $n_{tot} = L_{tot}/d = 951$. The volume V occupied by the nanoplates (based on the area of the field of view and the thermal fluctuation height of the nanoplates) was estimated as 7037 μm^3. The initial concentration of free silver nanoplates was therefore $[M]_0 \approx \frac{n_{tot}}{V \cdot N_A} = 2.24 \times 10^{-10}$ M, where N_A is Avogadro's constant (6.02×10^{23} mol^{-1}). The slope of the $\bar{X}_n - t$ curve in Figure 2C was fit as 0.0285 s^{-1} (R^2 = 0.99). As such, the assembly rate constant $k = \frac{0.0285}{4 \times 2.24 \times 10^{-10}} = 3.2 \times 10^7$ M^{-1}s^{-1}. Following the same analysis, we found that the total number of chains decreased gradually with time (due to the fusion of chains) and the mean chain length increased linearly with time, with a growth rate of 3.3×10^{-3} μm/s (Figure S5B).

It is important to note that our chain growth analysis started 330 s after adding NaCl to the unassembled system because, immediately after adding NaCl, we still observed particle diffusion in and out of the field of view. Consequently, we started the analysis after some time (namely 330 s) to ensure that the field of view was a nearly closed system, *i.e.*, with a constant total number of nanoplates (between 330 s and 630 s after NaCl addition, see Figure S5B). We expect that the particle diffusion immediately following the addition of NaCl also explains why the number-average degree of polymerization is not 1 if we extend the fitted curve to 0 s. However, this should not affect the calculation of the rate constant.

Flory−Schulz distribution fitting (Figures 2D and 3B)

The i-mer fraction (n_i/N_L) distribution present at a given time during step-growth polymerization can be described by a Flory−Schulz distribution.[7,8] Here, "i-mer" refers to a chain containing i nanoplates, and N_L is the total number of chains. Here we used $\frac{n_i}{N_L} = C(1-p)p^{i-1}$ to do the fitting, with p and C as fitting parameters. In this case, p is the extent of reaction at time t and C is a constant which accounts for the binning of the distribution. In particular, using the optical microscope, it is hard to determine accurately the exact value of i for a chain. As such, for each i-mer fraction histogram and each corresponding Flory−Schulz distribution fitting (Figures 3B and S6), we used $\bar{i}$, namely, the average i value in a local

series of i-mers (*e.g.* for a bin size of five we would consider $i-2, i-1, i, i+1$, and $i+2$ together), as one point in the horizontal coordinate, and the total number of i-mers in the range divided by N_{L} as the corresponding point in the vertical coordinate.

Note: for clarity in Figure 2D, the i-mer fraction histogram was adjusted very slightly in order to make the bars for each time point more distinguishable from one another. However, the Flory−Schulz fitting on this data was performed prior to this adjustment. We have also included all the original i-mer fraction histograms of step-growth polymerization in Figure S6.

The "chain stopper" model to predict interaction energy difference

The "chain stopper" model describes the step-growth polymerization of bifunctional monomers in the presence of monofunctional stoppers. Here, within the appropriate ionic strength range, silver nanoplates are the bifunctional monomers and Janus particles are the monofunctional stoppers.

Let c_{m} be the molar concentration of bifunctional silver nanoplates in the field of view, c_{s} be the molar concentration of monofunctional Janus particles, p be the extent of reaction of silver nanoplates, and p' be the extent of reaction of Janus particles.

Here we define: $p' = pe^{-\frac{|U_{\mathrm{mm}}-U_{\mathrm{ms}}|}{k_{\mathrm{B}}T}} = pe^{-\frac{|\Delta U|}{k_{\mathrm{B}}T}}$ (which accounts for the fact that nanoplates are less reactive with Janus particles than they are with other nanoplates), U_{mm} is the equilibrium nanoplate−nanoplate interaction energy, U_{ms} is the equilibrium nanoplate−Janus particle interaction energy, $\Delta U = U_{\mathrm{mm}} - U_{\mathrm{ms}}$, k_{B} is the Boltzmann constant, and T is the temperature.

After the system reaches equilibrium, the total number of chain ends is $2(1-p)c_{\mathrm{m}} + p'c_{\mathrm{s}}$.

Since the total number of chains N_{L} is equal to the total number of chain ends divided by 2, we get

$\bar{X}_{\mathrm{n}} = \frac{c_{\mathrm{m}}}{N_{\mathrm{L}}} = \frac{2}{2(1-p)+p'\frac{c_{\mathrm{S}}}{c_{\mathrm{m}}}} = \frac{2}{2(1-p)+\frac{c_{\mathrm{S}}}{c_{\mathrm{m}}}pe^{-|\Delta U|/k_{\mathrm{B}}T}}$.

As a quick check, when $c_{\mathrm{s}} = 0$, $\bar{X}_{\mathrm{n}} = \frac{1}{(1-p)}$. This is exactly the formula for step-growth polymerization of bifunctional monomers in the absence of monofunctional stoppers.

We calculated the number-average degree of polymerization $\bar{X}_{\mathrm{n}}$ using experimental data (by measuring the chain length in optical microscopy images and using a d spacing between neighboring nanoplates of 116.6 nm) in three conditions ($\frac{c_{\mathrm{s}}}{c_{\mathrm{m}}} = 0$, 1.2 and 3.5%). In each case, the extent of reaction p for silver nanoplates was obtained from fitting a Flory−Schulz distribution to the i-mer fraction distribution (Figure 3B).

The fitting equation is: $\bar{X}_{\mathrm{n}} = \frac{2}{2(1-p)+\frac{c_{\mathrm{S}}}{c_{\mathrm{m}}}pe^{-|\Delta U|/k_{\mathrm{B}}T}}$.

We used two variables to do the fitting and get ΔU. Here p and $\frac{c_{\mathrm{s}}}{c_{\mathrm{m}}}$ were the two independent variables, $\bar{X}_{\mathrm{n}}$ was the dependent variable, and $e^{-|\Delta U|/k_{\mathrm{B}}T}$ was the fitting parameter. The value of $e^{-|\Delta U|/k_{\mathrm{B}}T}$ obtained

from the fitting is 0.138 ± 0.056, with an R^2 equal to 0.99. The error is from the standard error of the fitting. The number-average degrees of polymerization $\bar{X}_n$ obtained from fitting this model show good agreement with experimental results for each concentration ratio condition, as shown in Table S3. Based on the fitted values of $e^{-|\Delta U|/k_B T}$, the interaction energy difference ($|\Delta U|$) is 1.6 $k_B T$ to 2.5 $k_B T$ at an ionic strength of 1.4 mM used in this particular experiment.

Theoretical determination of chain lattice constants

In order to corroborate the center-to-center spacing between neighboring nanoplates in the chain measured by SAXS and to verify that the extrapolated peak(s) q_1 corresponded to the chain lattice constants, we used an analytical solution for the interaction energy between two charged silver nanoplates to estimate the equilibrium chain lattice constant as a function of ionic strength. Interaction energies $U(d)$ were evaluated as a sum of an attractive van der Waals potential[9] and a repulsive electrostatic potential,[10] that is, $U(d) = U_{\mathrm{vdW}}(d) + U_{\mathrm{el}}(d)$, where

$$U_{\mathrm{vdW}} = -\frac{HA_{\mathrm{plate}}}{12\pi}\left[\frac{1}{\left(d - t_{\mathrm{plate}}\right)^2} - \frac{2}{d^2} + \frac{1}{\left(d + t_{\mathrm{plate}}\right)^2}\right]$$

and

$$U_{\mathrm{el}} = \frac{\varepsilon\varepsilon_0\zeta^2 A_{\mathrm{plate}}}{b}\left[1 - \tanh\left(\frac{d - t_{\mathrm{plate}} - 2t_{\mathrm{ligand}}}{2b}\right)\right].$$

Here, d is the center-to-center spacing between two neighboring nanoplates, t_{plate} is the nanoplate thickness, and A_{plate} is the projected surface area that two nanoplates have in common. The variable H is the Hamaker constant for silver and silver interacting across water.[11] In the electrostatic potential, ε is the relative permittivity of water, ε_0 is the vacuum permittivity, ζ is the zeta potential of the thiol-coated silver nanoplates in water, and b is the Debye length, given (in nanometers) for an aqueous solution of sodium chloride salt as $b = \frac{0.304}{\sqrt{I}}$ for ionic strength I (in moles per liter). In addition, t_{ligand} is the thickness of the carboxylate−thiol monolayer on the nanoplate surface.[12,13] The area was approximated as $A_{\mathrm{plate}} = \frac{a^2\sqrt{3}}{4}$ for nanoplates with edge length a. Here we assumed that the two nanoplates are in a perfectly aligned, face-to-face configuration.

Net interaction potentials and the locations of their secondary minima at different ionic strength conditions are indicated in Figure S7, as calculated using the values in Table S6. For the interaction calculation of two nanoplates with different edge lengths, the area A_{plate} is essentially the surface area of the smaller nanoplate's face.

Depletion attraction calculation

From the synthesis of nanoplates which have an edge length suitably large for optical microscopy imaging, there is also a small fraction of smaller particles. To determine whether or not these smaller nanoplates were able to act as depleting agents (and therefore enhance the assembly of larger nanoplates), we conducted a simple estimation of this interaction strength for a sample characteristic of those used in studying nanoplate self-assembly (*i.e.*, where the larger nanoplates have an edge length of 1.44 μm on average).

The depletion attraction is given by $U_{\mathrm{dep}} = -\rho \Delta V k_{\mathrm{B}} T$.[9,14] Here, ρ is the number density of the depletant (here, the smaller nanoplates), and ΔV is the volume gained by the depletants due the overlap of exclusion layers when two larger nanoplates assemble face-to-face.

The number density of larger nanoplates is $\frac{951\ particles}{7037\ \mu m^3} = 0.135$ particles/μm^3 (see the assembly rate constant discussion above). The number of smaller nanoplates (with an average size of 0.51 μm) is around 32% the number of larger nanoplates (see Figure S1D). Thus, the number density of smaller nanoplates is about 4.32×10^{-2} particles/μm^3. At 1.4 mM ionic strength condition, the center-to-center spacing between two neighboring nanoplates is 116.6 nm. We calculated the overlapping volume as $\Delta V = 2\times\frac{\sqrt{3}}{4}\times 1.44^2 \times (510 - 116.6)\times 10^{-3}$ μm^3 = 0.71 μm^3, assuming the maximum possible excluded layer thickness (corresponding to the edge length of the smaller nanoplates) and thus the maximum possible depletion attraction. As a result, $U_{\mathrm{dep}} = -\rho \Delta V k_{\mathrm{B}} T = -4.32\times 10^{-2}\times 0.71\ k_{\mathrm{B}} T = -0.03\ k_{\mathrm{B}} T$. Compared with the net interaction strength calculated by considering only van der Waals and electrostatic potentials, which is $-35\ k_{\mathrm{B}} T$ (Figure S7B), the depletion attraction caused by the presence of smaller particles is negligible.

Interchain interaction discussion

The lateral interactions between two individual nanoplates or between assembled chains in the relatively low ionic strength conditions (*i.e.*, 1.4 mM) we used to study the self-assembly of nanoplates are most likely negligibly small compared to the interactions associated with the face-to-face assembly of two nanoplates. In particular, using the same equations for the van der Waals attraction and electrostatic repulsion as an estimate, the net interaction strength scales with the projected surface area that two nanoplates have in common. Nanoplates only have a ~30 nm thickness (in contrast with a 1.44 μm edge length), and so the projected surface area between two laterally approaching nanoplates (or for edge-to-face assembly), even in perfect alignment, is only ~5% of the surface area involved in face-to-face assembly. For the lateral approach of two chains, the relevant surface area is also greatly reduced compared to face-to-face assembly because of the large separation between neighboring nanoplates (~117 nm at 1.4 mM, making chains "holey" along their length) and the fact that nanoplates in the chains fluctuate laterally. Given the short range of van

der Waals attraction, these "curved-out" regions of the chain likely contribute very little to any attraction that two chains approaching side-by-side experience (Figures 2A and S4).

Chain fluctuation analysis

A variety of methods can be used to characterize the transverse fluctuations of colloidal chains observed under optical microscopy. One can analyze the power spectra of chain oscillations,[15-17] determine various chain fractal dimensions (such as the "box-counting" dimension, a perimeter- or area-based fractal dimension, *etc.*),[18] or probe various scaling relationships.[19,20] Many of these approaches are ultimately linked.[18,21] Here we employed the last of these and determined the so-called "roughness" or "Hurst" scaling exponent for chains in solutions of different ionic strengths. It has been argued that this characterization can hold up well against resolution effects[18,22] if single-particle detection is not possible.

The roughness exponent is associated with the scaling of the height−height correlation function. In particular, if $h(x,t)$ refers to the transverse height h at a point x along a chain's backbone at time t, the height−height correlation function can be written as $C(x,x') = \langle (h(x) - h(x'))^2 \rangle^{1/2}$. There is typically a defined regime where this function follows a power-law form, or $C(x,x') \propto |x - x'|^{\alpha}$ where α is the roughness exponent.[19-21] In other words, the roughness exponent describes how different the heights of two points are as a function of how far apart they are along a chain at a particular time.

To perform this characterization, it was first necessary to formulate a height function $h(x,t)$ for a chain. We did so mostly following a method employed by Silva *et al.*, involving frame-wise image analysis of optical microscopy movies.[20] A chain of interest was first selected by cropping to the relevant area and then aligned between frames using the built-in ImageJ/FIJI registration algorithm "StackReg" in order to reduce any motions between frames due to global movement of the chain in solution, *e.g.* by rotation or migration across the field of view. Specifically, the "rigid body" setting of StackReg corrects for rotation and translation between frames while preserving shape and scale. Each chain was then binarized and skeletonized, again using built-in ImageJ/FIJI functionalities ("Make Binary" and "Skeletonize" under the "Binary" submenu) in order to trace the center line of the chain (only the silver chain segment, not including the Janus particles on chain ends) in each frame to a width of one pixel. The resulting pixel positions were used to formulate frame-specific height functions $h(x)$ (Figures 4A and S20). Four chains were considered in this way for each ionic strength condition. Height correlation functions for each chain are plotted in Figure S21 and roughness exponents for each chain considered are given in Table S4. We found an average roughness exponent α = 0.737 ± 0.011 for chains fluctuating in 1.4 mM ionic strength solutions and an average α = 0.679 ± 0.087 for chains in 3.0 mM ionic strength solutions, with errors corresponding to the standard deviation among different chains. Figure 4D was prepared by averaging the four roughness

exponent curves for each ionic strength condition first and fitting a line to the linear regime of the log−log plot (*i.e.*, a power law relationship). The fitted roughness exponent values were very similar, with α = 0.736 ± 0.018 at 1.4 mM and $\alpha = 0.656 \pm 0.013$ at 3.0 mM, with errors from the standard error of the fitting (Figure 4D).

An exponent $\alpha > 0.5$ describes a positively correlated random walk in the lateral direction or "fractional" Brownian motion.[20] Volume exclusion between nanoplate "monomers" prevents appreciable bending of the chain, but nanoplates can fluctuate by sliding against one another in the lateral direction. Since the relative separation $|x - x'|$ is proportional to the number of nanoplates in a segment of this length, the roughness exponent is associated with the ability of such a segment to extend out of lateral alignment in a net manner (*i.e.*, out of a perfectly straight chain) due to nanoplates sliding past one another. At a lower ionic strength (1.4 mM), since nanoplate−nanoplate repulsions are stronger (and the net attraction at their equilibrium position is weaker), there is a lesser enthalpic penalty (from reduction in the projected surface area that two nanoplates have in common) for lateral displacement and chains can extend more in the lateral direction, leading to a larger exponent ($\alpha \approx 0.736$). Meanwhile, at higher ionic strength (3.0 mM), the roughness exponent is smaller ($\alpha \approx 0.656$) because attractions are stronger. This interpretation of the difference in roughness exponent between ionic strength conditions is also consistent with the observations that (i) at a lower ionic strength, particular points on a chain deviate more over time and (ii) the "step size" (*i.e.*, the height difference) distribution for chains in solution with lower ionic strength tends towards larger "steps" (Figures S12 and S22).

Energetic considerations of lateral fluctuation

When nanoplates slide past one another within the chain (Figure S12A), based on the model we used for the interaction energy between two nanoplates, the equilibrium center-to-center d spacing will remain unchanged but the net attraction strength will be reduced because the projected surface area that two nanoplates have in common is reduced. The net attraction is at a maximum when two nanoplates are fully aligned, but goes to zero as nanoplates slide past one another. To estimate the scale of the interaction energy reduction due to lateral offset of nanoplates in the chain, we calculated the net attraction between two nanoplates for varying degrees of lateral offset using the same potentials as detailed above. The result is shown in Figure S12B. We then used this calculation to estimate a relative probability for varying degrees of lateral offset between two nanoplates based on a Boltzmann distribution. In other words, we calculated the relative probability of a lateral offset as $p_{\mathrm{rel}} \approx e^{-(U_{\mathrm{offset}} - U_{\mathrm{aligned}})}$ where U_{offset} is the equilibrium attraction for some degree of lateral offset and U_{aligned} is the equilibrium attraction with no lateral offset (Figure S12C). We then compared this relative probability with frequencies of particular degrees of lateral

offset observed in experiments. The lateral offset distribution determined from optical microscopy is based on the height offset between two points one pixel away along a chain's backbone, combining data from each of the four chains analyzed in each ionic strength condition. We normalized this distribution of $h(x+1)-h(x)$ about zero (namely, we set the frequency of no lateral offset as 1) and plotted it together with the Boltzmann probability (Figure S12C). Based on this Boltzmann idea, nanoplates are energetically allowed to slide past one another by a few tens of nanometers at both ionic strengths, consistent with the lateral offsets in the range of tens of nanometers from our fluctuation analysis. Note that the nanoplates in the chain have a slightly larger lateral offset than what the Boltzmann distribution predicted at both ionic strengths. We propose three possible reasons for this larger lateral offset here. First, probability distributions of $h(x+1)-h(x)$ are only a rough estimate of lateral offset between individual nanoplates, since the optical microscope is unable to resolve accurately individual nanoplates within a chain. Second, the energy reduction due to lateral offset is calculated based on two nanoplates in an otherwise perfectly aligned, face-to-face configuration (Figure S12A). This energy reduction is smaller at the same degree of lateral offset if the two nanoplates are not in a perfectly aligned face-to-face configuration. Third, for the images from optical microscopy, one pixel size is ~74 nm. The lateral offset measurement is not very accurate due to the limited resolution of the optical microscope.

Persistence length calculations

For each of the eight chains analyzed above (four chains in each ionic strength condition), we also calculated a persistence length, L_p. The persistence length is a measure of the flexibility of a chainlike object and can be defined as the length scale beyond which vectors tangent to the chain contour lose their correlation.[8,15] We calculated persistence lengths using an image analysis-based technique involving the decomposition of the instantaneous curvature of a chain into independent Fourier modes.[15,16,23] To begin, the height function of a chain, $h(x,t)$ (determined as described above) was converted into an angle function, $\vartheta(s,t)$, where each point is given by

$$\vartheta(s_m,t)=\tan^{-1}\left[\frac{h_{m+1}-h_m}{x_{m+1}-x_m}\right]$$

and s_m is given by

$$s_m=\left(\sum_{j=0}^{m-1}\sqrt{\left(x_{j+1}-x_j\right)^2+\left(h_{j+1}-h_j\right)^2}\right)$$

In other words, $\vartheta(s,t)$ describes the tangent angle at a contour length s along the chain.

The function $\vartheta(s)$ for each time t can then be decomposed into a series of independent Fourier cosine modes, or,

$$\vartheta(s) = \sum_{\mu=0}^{\infty} \vartheta_\mu(s) = \sqrt{\frac{2}{L}} \sum_{\mu=0}^{\infty} a_\mu \cos\left(\frac{\mu \pi s}{L}\right)$$

Where L is the length of the chain, μ is the mode number, a_μ is the amplitude of mode μ, and s is again the contour length from the end of the chain. We calculated this decomposition for each chain at each time point using the "DCT-I" function in MATLAB. Each mode in this decomposition gives an independent estimate of the persistence length of the chain, given by $L_\mathrm{p} = \frac{L^2}{\mu^2 \pi^2 \,\mathrm{var}(a_\mu)}$ where $\mathrm{var}(a_\mu)$ refers to the variance of the mode μ amplitude over the 100 collected angle functions (*i.e.*, one for each of 100 frames) for each chain. However, this equation only holds within a certain range of modes, beyond which noise in the image or the skeletonization procedure leads to significant errors in the determination of a_μ.[15,16,23] This effect is depicted graphically in Figures S13A and B; beyond some μ, plotting $\log(\mathrm{var}(a_\mu))$ *versus* $\log(\mu)$ no longer gives a slope of −2, as indicated in the equation above for the persistence length. Thus, for each chain, we only considered data points with a good approximation of −2 power law relationship ($R^2 > 0.83$, Figure S13C).

Using the selected range of modes for each chain, we calculated mode-specific persistence lengths (Figure S13D) and averaged the persistence lengths for different modes for each chain. The detailed contour length and persistence length values for each chain are also listed in Table S4. The persistence length calculated for each chain is much larger than the contour length of the chain, in all cases by about one order of magnitude or more. Thus, all chains are essentially unbending and "rigid".

Figures S1−S22

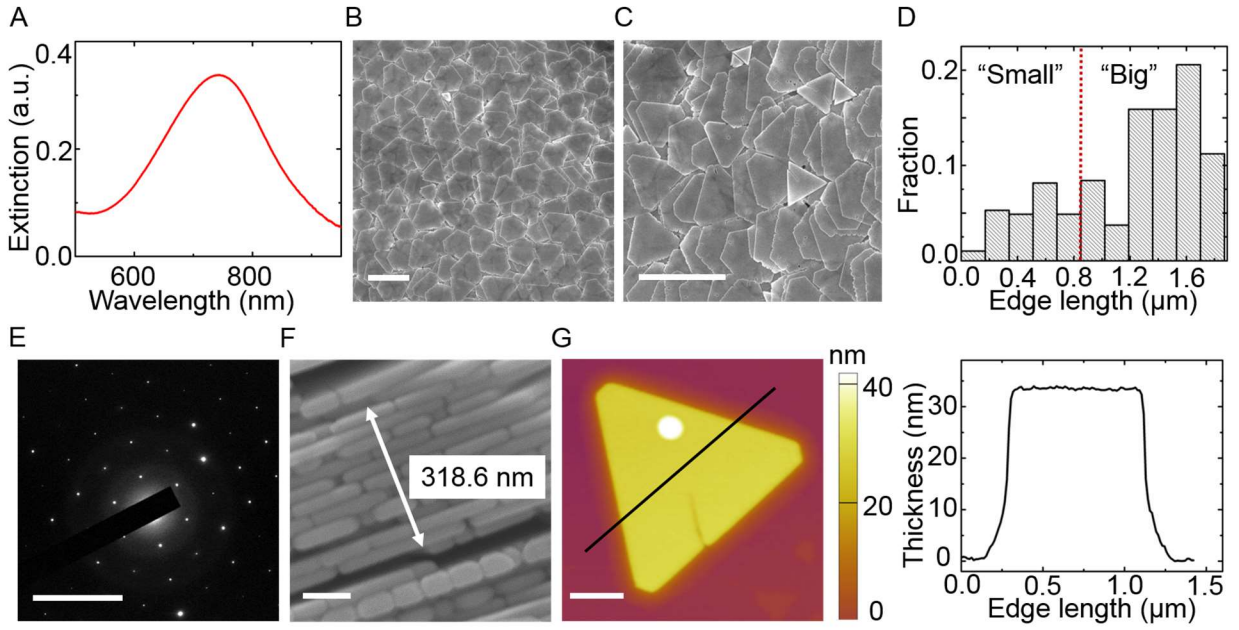

Figure S1. Characterization of silver nanoplates (edge length: 1.44 ± 0.26 μm, considering only the big assembling nanoplates) used in the experiments associated with Figures 2, 3, 4 and 5A. (A) A typical UV−vis spectrum measured from a solution of as-synthesized silver seeds. (B) Low- and (C) high-magnification SEM images of silver nanoplates. (D) The size distribution of silver nanoplates measured from SEM images using ImageJ. Here we set nanoplates with edge length smaller than 60% of the big nanoplates as small nanoplates (edge length smaller than 0.85 μm, see the dotted red line). As such, the small nanoplates have a size distribution of 0.51 ± 0.20 μm (namely 22% to 49% the size of the big nanoplates). The fraction of small nanoplates is about 32% compared with big nanoplates. (E) The SAED pattern of a representative silver nanoplate indicates that they are single crystalline. (F) The nanoplate thickness measured from an SEM image of standing stacked silver nanoplates. The measured thickness is 29 ± 4 nm, based on thickness measurements of 11 nanoplates in this image. This thickness value was used for interaction calculations, see Table S6. (G) AFM image (left) and (right) the corresponding thickness profile (across the black line in the left-hand image) of a representative silver nanoplate. Scale bars are: 2 μm in (B) and (C), 10 nm^{-1} in (E), 100 nm in (F), 300 nm in (G).

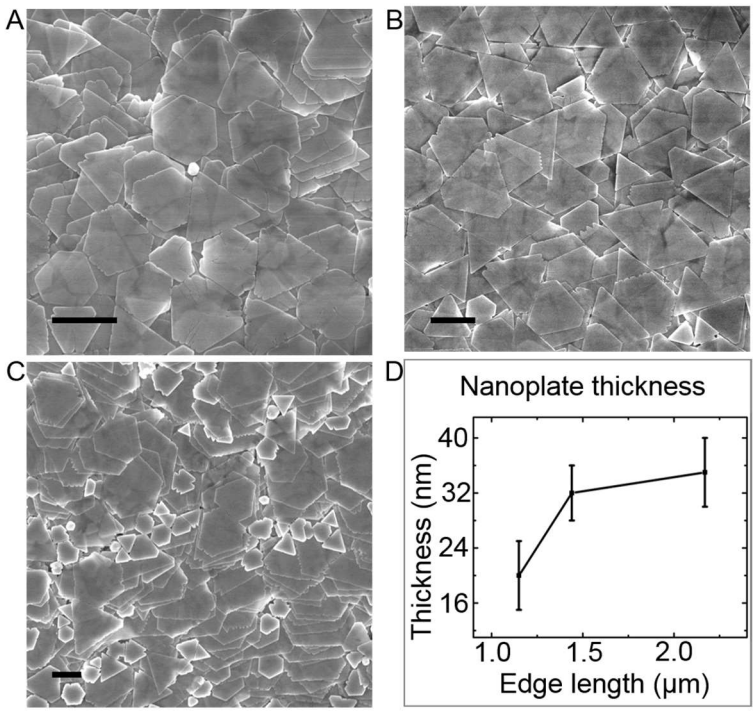

Figure S2. SEM images and thickness of silver nanoplates of different edge lengths. (A) – (C): SEM images of silver nanoplates of different edge lengths. (A) Edge length: 1.09 ± 0.14 μm, (B) 1.46 ± 0.22 μm and (C) 2.17 ± 0.33 μm. The edge length measurement does not include the much smaller particles in the system, as these very small particles are typically not involved in assembly. Scale bars: 1 μm. (D) Thickness of silver nanoplates of different edge lengths measured by AFM. The error bars shown in (D) are determined from averaging different particles in the same batch. See the synthesis details in Table S1.

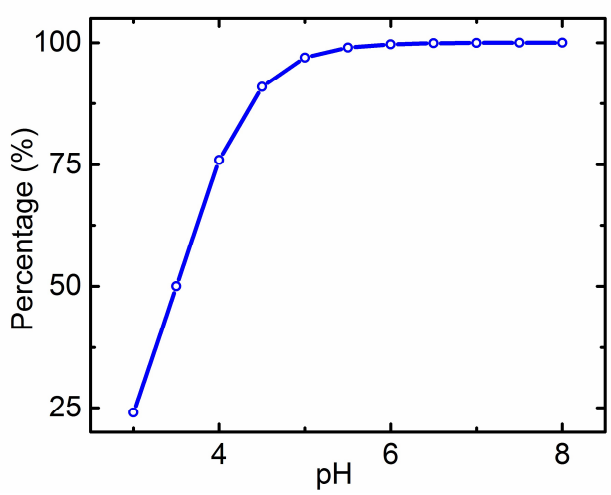

Figure S3. Calculated percentage of deprotonated carboxylate−thiol ligands on the silver nanoplate surface as a function of pH. A value of 3.5 was used for the pK_a of carboxylate−thiol ligands, based on information from the manufacturer.

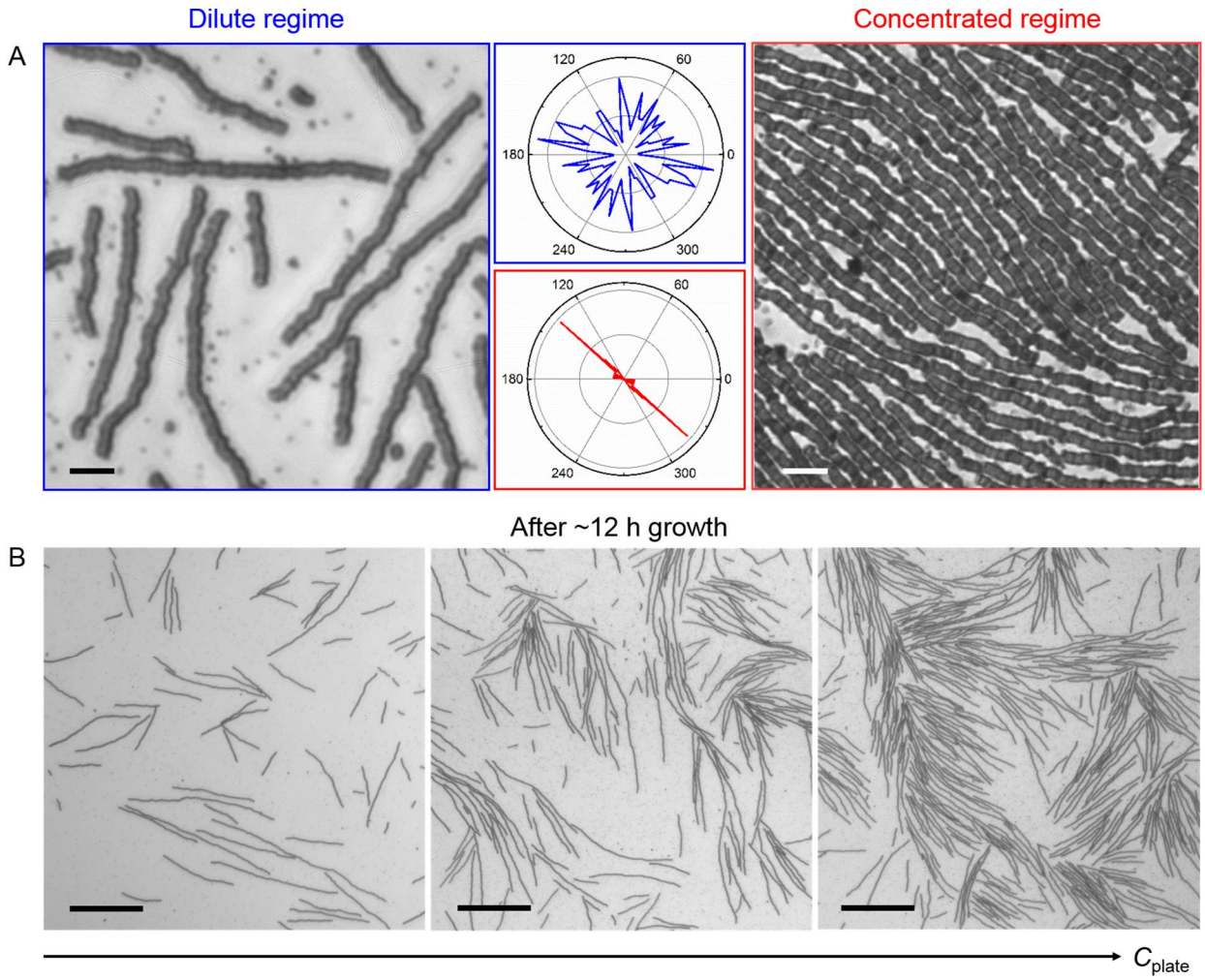

Figure S4. Optical microscopy images of chains self-assembled in solutions with different nanoplate concentrations and corresponding 2D radial order distribution plots.[24,25] (A) Typical optical microscopy images of chains assembled from a solution with a low (far left) and a high (far right, same image as shown in Figure 2A, slightly zoomed-out view) concentration of silver nanoplates and (center) the corresponding 2D chain orientation distribution plots (The blue curve corresponds to the dilute regime and red curve corresponds to the concentrated regime. Units are in degrees). The 2D radial order distribution plots are based on assigning vectors to the colloidal chains. For the dilute radial order distribution plot, four images at the similar region were used together to obtain enough statistics. (B) Chains grow to more than 100 μm after ~12 h growth at different nanoplate concentration regimes. Ionic strength: 1.4 mM. Scale bars: 5 μm in (A) and 50 μm in (B).

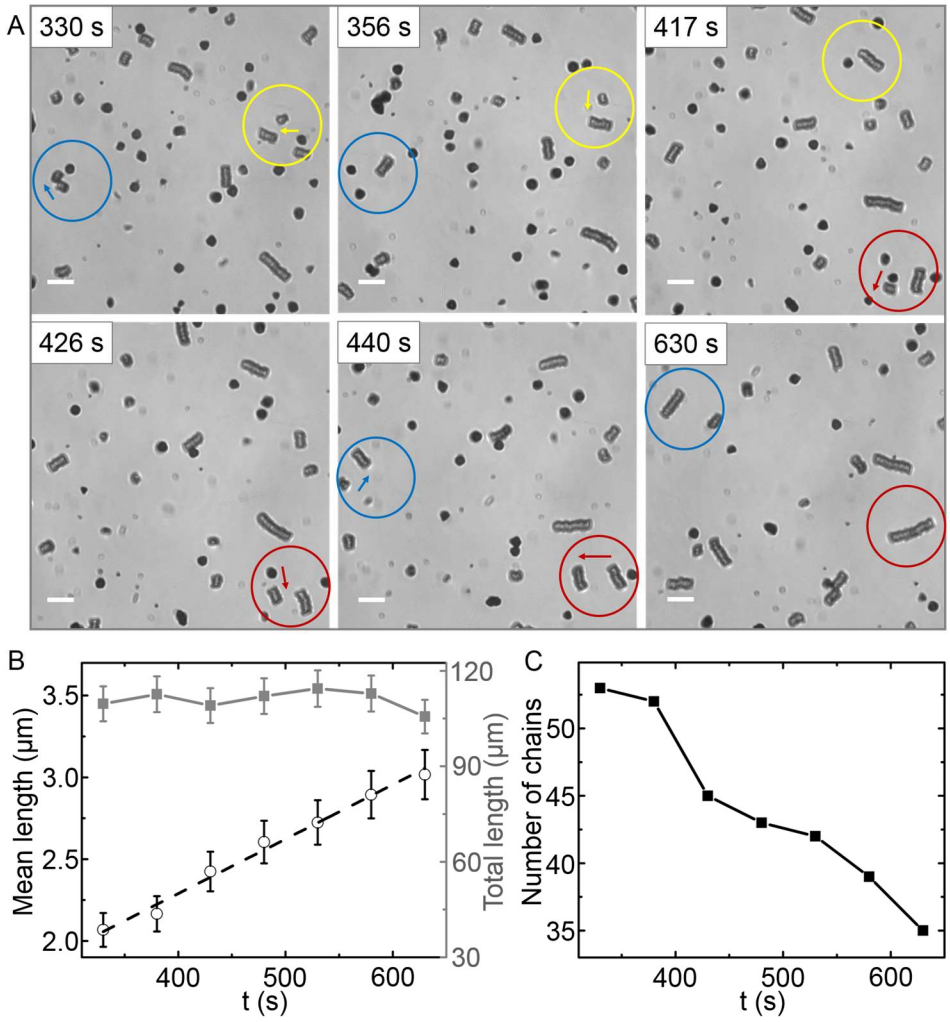

Figure S5. Step-growth polymerization of bifunctional nanoplates. (A) Time-lapse optical microscopy images of the silver chain growth process in the early growth stage (330 s to 630 s after adding NaCl solution to screen electrostatic repulsion between nanoplates) showing the step-growth polymerization mechanism (Figures 2C and 2D). Different circles represent the growth of different chains, with the arrows highlighting the chain addition. Ionic strength: 1.4 mM. Scale bars: 5 μm. (B) Mean chain length growth (black circles) and total chain length (grey squares) in the field of view over time. The linear fitting (black dotted line) gives a growth rate of 3.3×10^{-3} μm/s ($R^2 = 0.99$). The error bars are from measurement errors. (C) Total number of chains in the field of view as a function of time. Due to the limited resolution of the optical microscope, we neglected measurements of very short chains (chain length < 1 μm) which could not be distinguished from single nanoplates during analysis. These short chains or single nanoplates are ~8% compared with all the chains in the field of view.

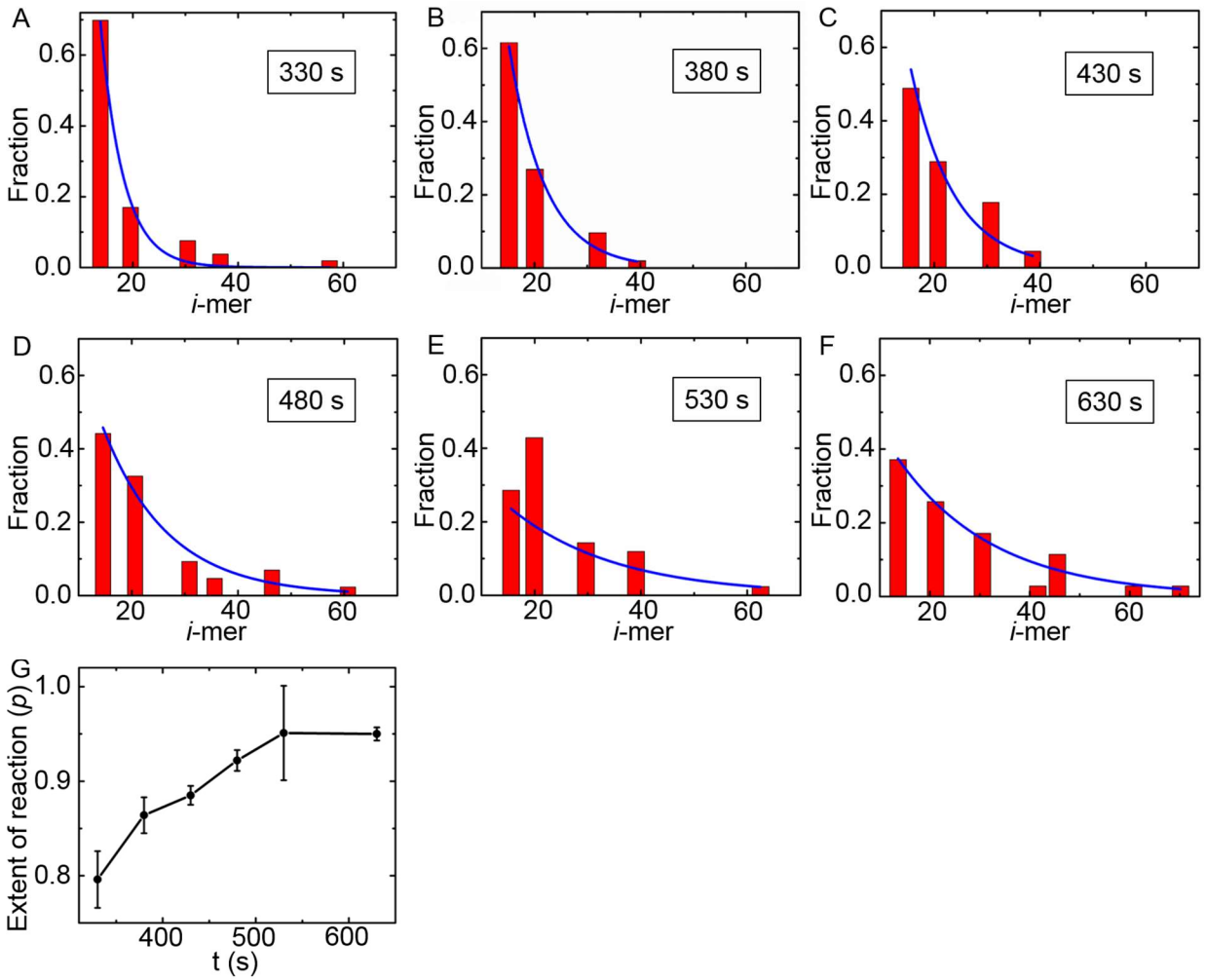

Figure S6. The i-mer fraction distributions at different stages of self-assembly and their corresponding Flory−Schulz distribution fitting (blue curves). (A) 330 s, (B) 380 s, (C) 430 s, (D) 480 s, (E) 530 s, (F) 630 s. The bin size is ~8.6. The first binning starts from 8.6 to 17.2, since the smallest i measured is 8.6 (corresponding to a chain of 1 μm long). (G) The extent of reaction (p) determined from the Flory−Schulz distribution fitting at different times. The error bars are from the standard error of the Flory−Schulz distribution fitting.

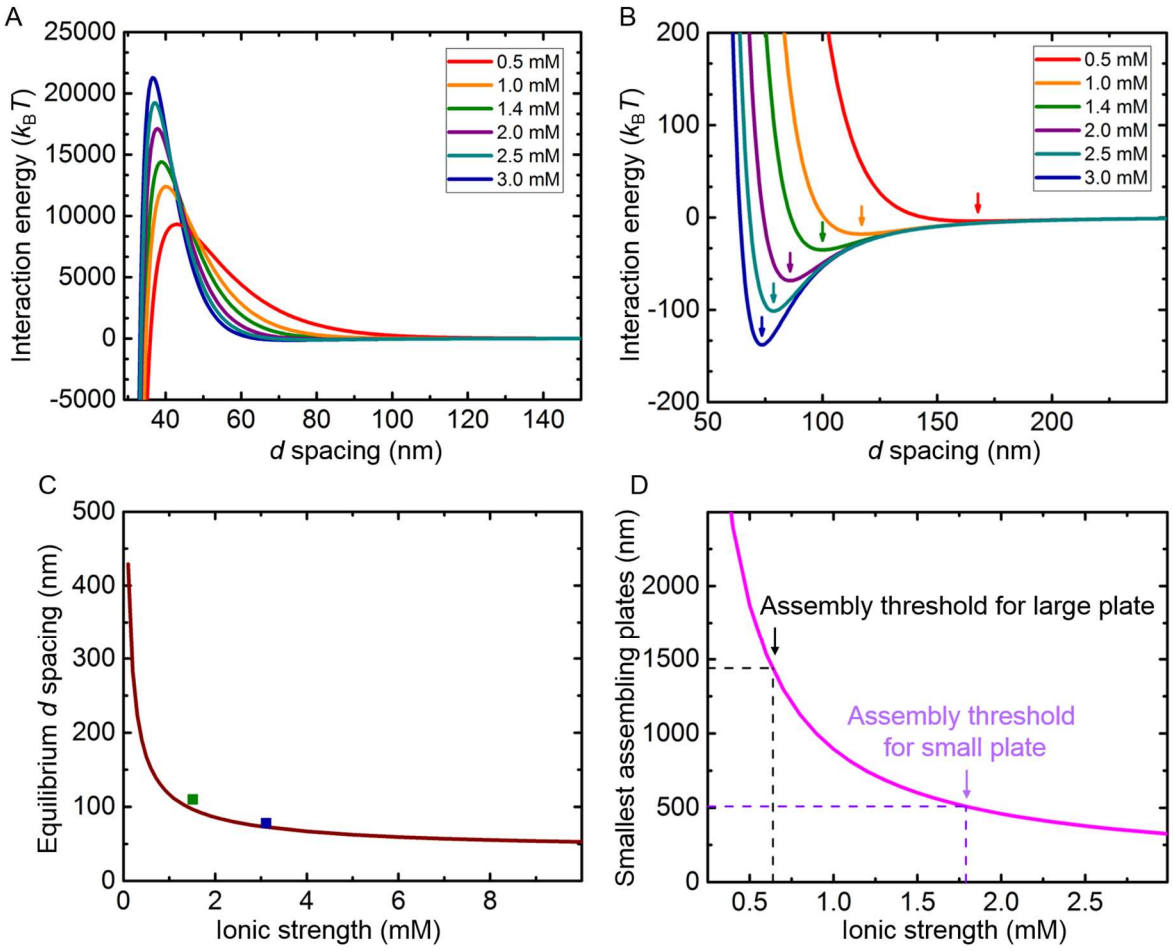

Figure S7. Interaction potential calculations and equilibrium center-to-center d spacings of two face-to-face assembled silver nanoplates. (A) Net interaction energy as a functional of center-to-center d spacing between two silver nanoplates at different ionic strength conditions. (B) A zoomed-in version of the plot in (A) showing the location of secondary energy minima at the equilibrium center-to-center d spacing. (C) The locations of secondary minima (namely the equilibrium center-to-center d spacing between two nanoplates) as a function of ionic strength (brown curve). The two squares mark measurements by SAXS at 1.4 (green) and 3.0 mM (blue), indicating decent agreement between the calculations and SAXS measurements. (D) The smallest assembling nanoplates at different ionic strength conditions. Here we set the secondary energy minima strength of at least $-7\ k_B T$ for a stable face-to-face assembly of nanoplates.[2] For interaction calculations of different size nanoplates, all the parameter values are same as (A), also listed in Table S6, except changing the surface area A_{plate}. For example, for a typical edge length of 1.44 μm, an ionic strength of at least 0.7 mM is needed for assembly (black dotted lines), which is also consistent with experimental observations (~0.8 mM); for assembly of small nanoplates (*i.e.*, 0.51 μm edge length), an ionic strength of at least 1.8 mM is needed (lavender dotted lines).

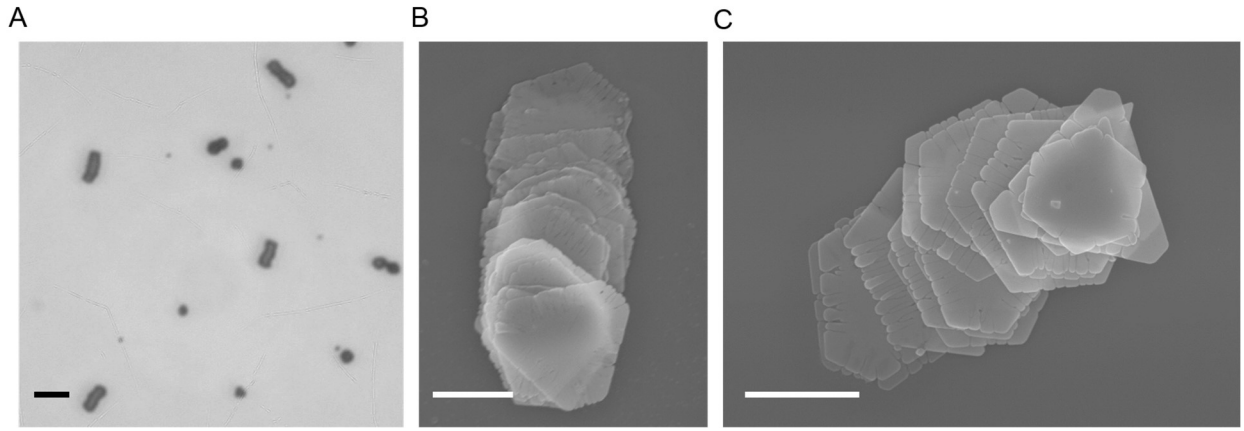

Figure S8. Characterization of assembled chains before and after solvent evaporation. (A) An optical microscopy image of assembled chains in 1.6 mM ionic strength solution (below the assembly threshold ionic strength of 1.8 mM for small nanoplates, based on the interaction calculation, see Figure S7D) before solvent evaporation. (B) and (C): SEM images of the assembled chains after rapid solvent evaporation under vacuum condition. The SEM images show that the assembled chains at this ionic strength condition (1.6 mM) are primarily composed of large nanoplates of similar size (*i.e.*, those with edge lengths of 1.44 ± 0.26 μm, see also Figure S1). Scale bars are: 5 μm in (A), 1 μm in (B) and (C).

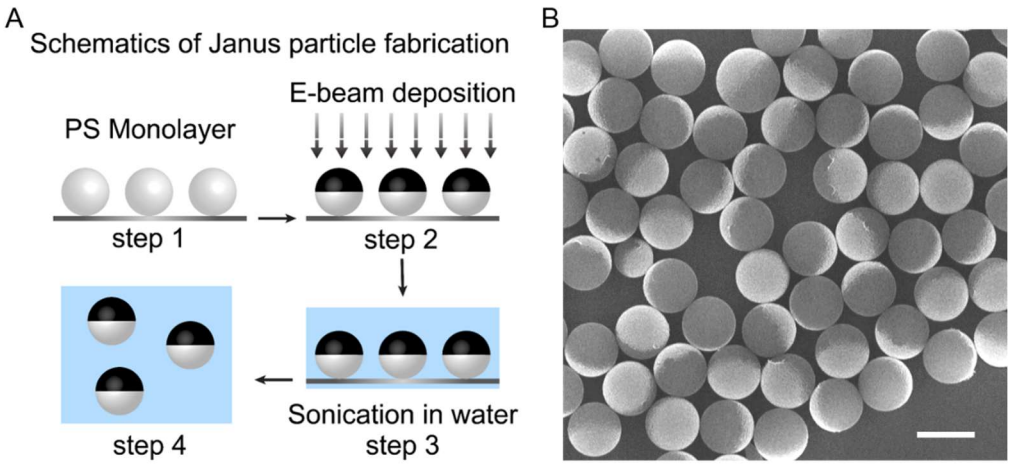

Figure S9. Janus polystyrene (PS) particles with a diameter of 2 μm. (A) Schematics of the Janus particle preparation process, which includes four steps: 1) Depositing a PS particle monolayer on glass slide; 2) Applying a 2 nm titanium and a 15 nm gold coating on one side of the particle by e-beam deposition; 3) Collecting Janus particles from the glass slide by sonication in water; 4) Dispersed Janus particles in water. (B) An SEM image of the prepared Janus particles. The bright side on the particle is the gold side and the dark side is the polystyrene side. Scale bar: 2 μm.

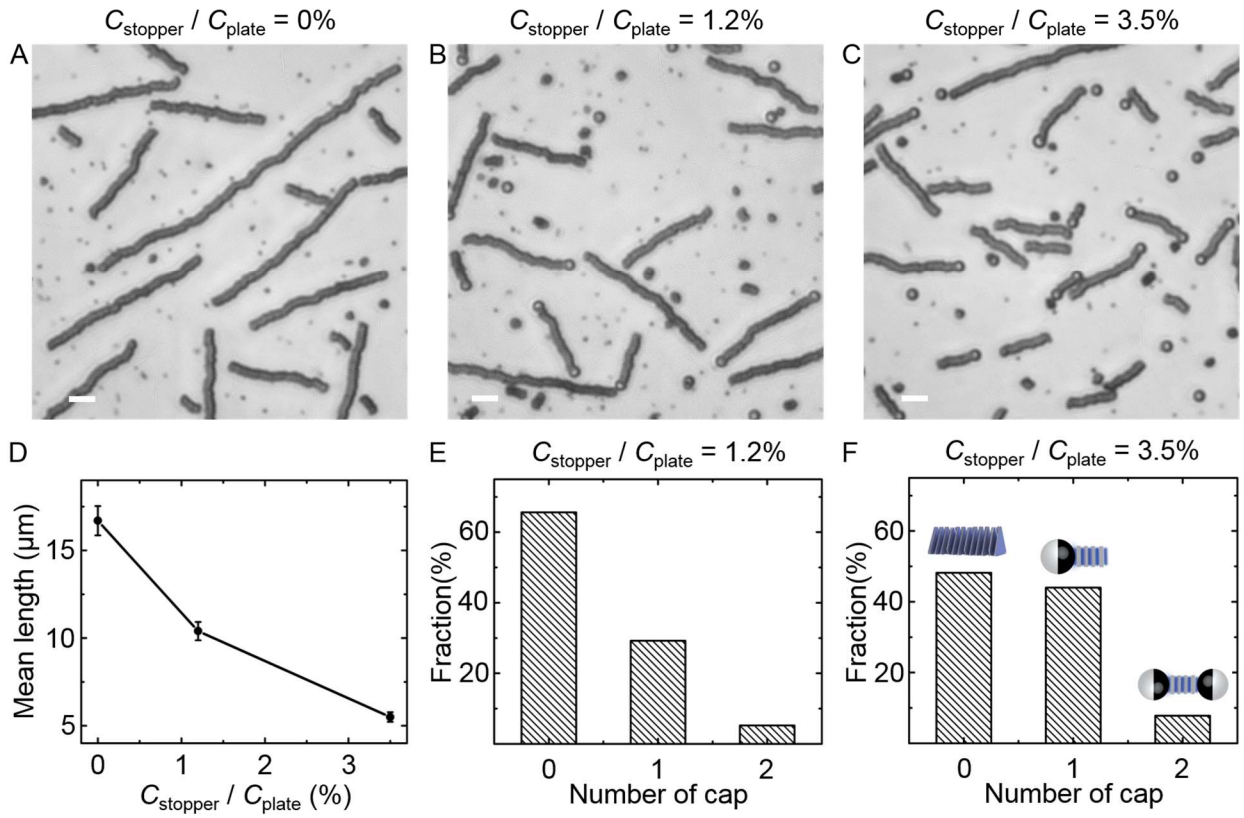

Figure S10. Janus particles as chain stoppers. Representative optical microscopy images to show the control over chain lengths through co-assembly of silver nanoplates with Janus particles (stoppers) at different Janus particle−nanoplate concentration ratios (the same images as the insets in Figure 3B but a larger view). (A) No Janus particles added. All chains grow without hindrance. (B) A relatively low Janus particle−nanoplate concentration ratio of 1.2%. Most chains have their growth halted by Janus particle stoppers. (C) A relatively high Janus particle−nanoplate concentration ratio of 3.5%. Chains tend to be even shorter, as more Janus particles are added for chain stopping. Ionic strength: 1.4 mM. Scale bars: 5 μm. (D) Mean chain length at different Janus particle−nanoplate concentration ratios. The error bars are from measurement errors. The distribution of chains capped with different number of Janus particles (0, 1, and 2, see the corresponding schematics inset in (F)) on the chain ends, at a low Janus particle−nanoplate concentration ratio of 1.2% (E) and high Janus particle−nanoplate concentration ratio of 3.5% (F). Note: The schematics inset in (F) are not drawn to scale.

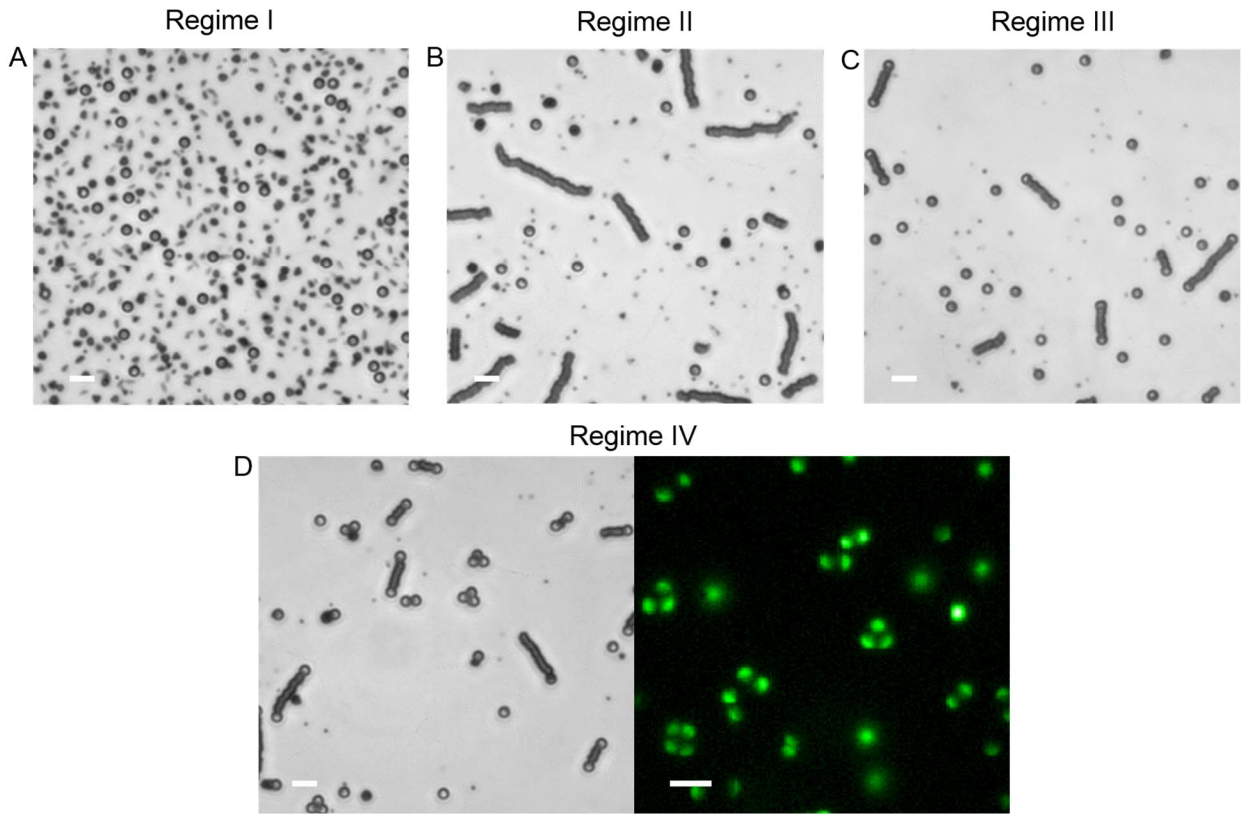

Figure S11. Representative optical microscopy images of the assembly of a binary mixture of silver nanoplates and Janus particles in different ionic strength regimes (Figure 3A). (A) No assembly (Regime I). Ionic strength: 0.3 mM. (B) Nanoplate-only chains and dispersed Janus particles (Regime II). Ionic strength: 0.8 mM. (C) The desired co-assembly regime, where Janus particles are attached to the silver chain ends (Regime III). Ionic strength: 1.4 mM. (D) Janus clusters (Regime IV). The left is a bright-field optical microscopy image and the right is a fluorescence microscopy image highlighting the Janus clusters. Ionic strength: 3.0 mM. Scale bars: 5 μm.

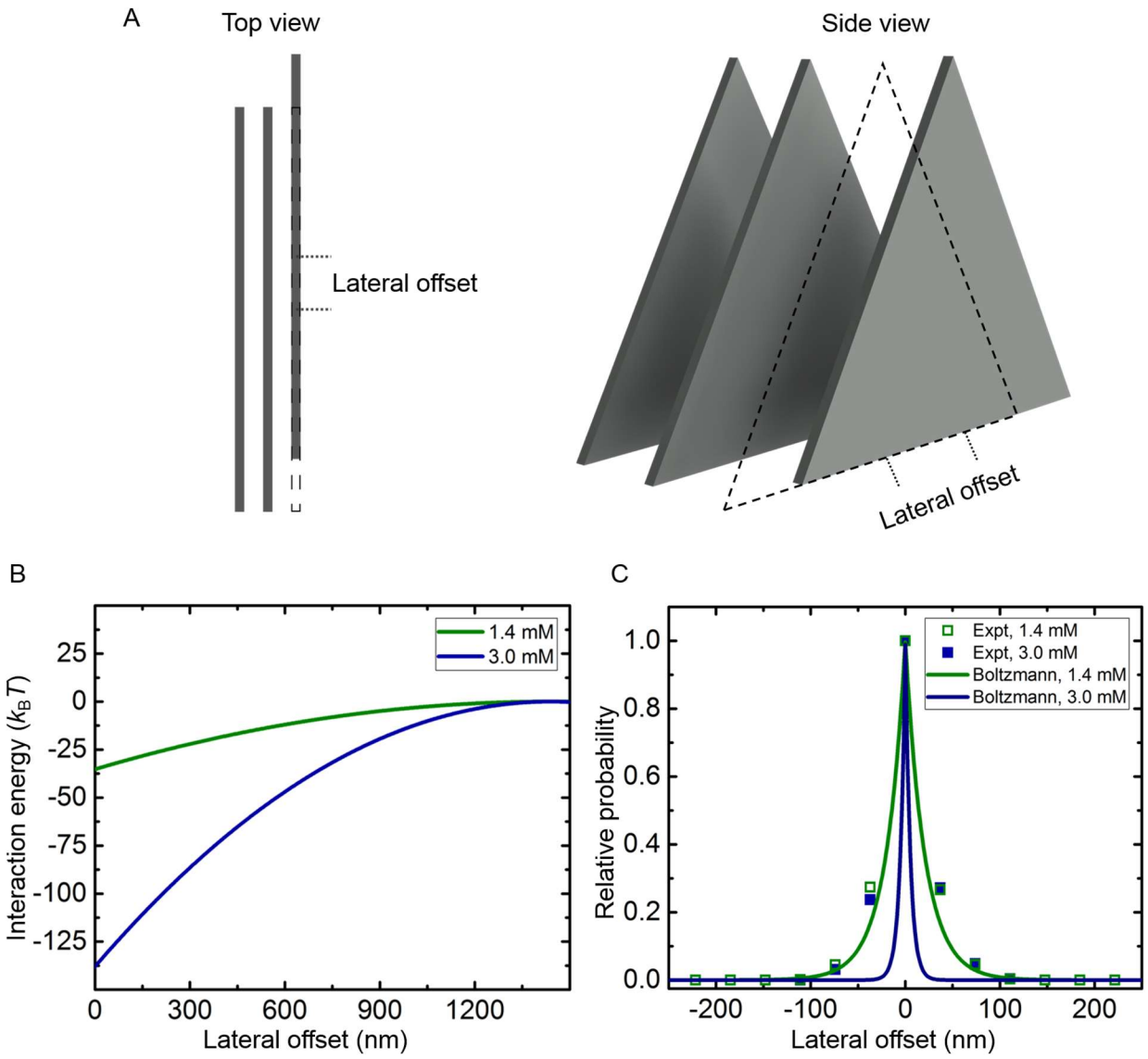

Figure S12. Interaction energy and probability of chain lateral offset. (A) Schematics (not to scale) of nanoplate lateral offset in a chain due to "sliding" away from the central position. Left: top view. Right: side view. (B) A plot showing the interaction energies at the equilibrium center-to-center spacing as a function of lateral offset distance at two ionic strength conditions. (C) Relative probability at different lateral offset distances at two ionic strength conditions, based on a Boltzmann probability distribution. The squares in the plot are the experimentally observed distribution of $h(x+1) - h(x)$ normalized to zero offset (*i.e.*, such that $h(x+1) - h(x) = 0$ has relative probability of 1) for each ionic strength condition, for qualitative comparison.

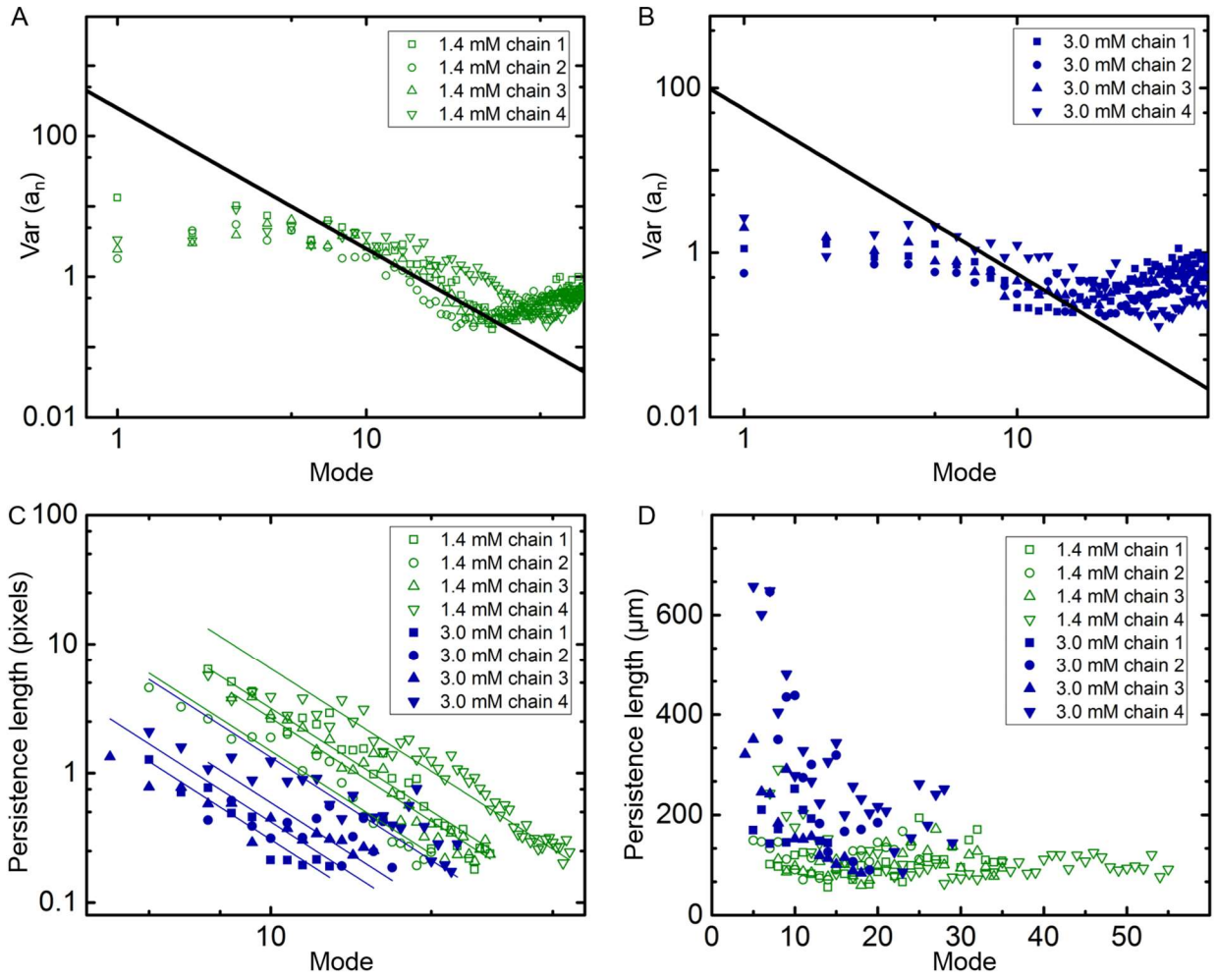

Figure S13. Persistence length analysis. (A) and (B) The log−log plots showing the variance of the mode amplitude as a function of the mode number for eight chains across the persistence length spectrum at (A) 1.4 and (B) 3.0 mM ionic strength conditions. The black lines in (A) and (B) have a slope of −2, indicating the regime(s) where the relation between mode number and persistence length applies. (C) Linear fitting of the curves in (A) and (B) at the low mode regions. Pixel size: 1/73.86 nm. (D) Persistence length as a function of the mode number for eight chains analyzed. The persistence length values for each chain are also listed in Table S4.

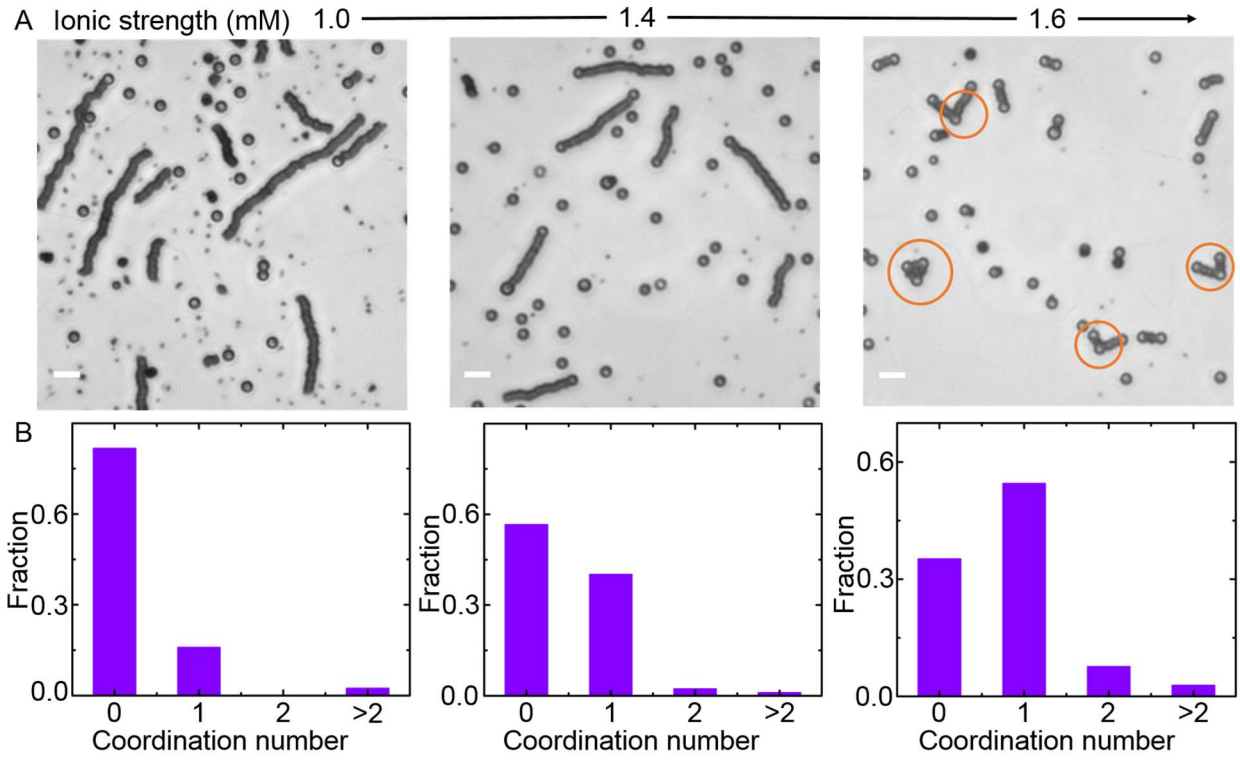

Figure S14. Janus particle coordination number distribution at different ionic strengths. (A) Typical optical microscopy images of structures assembled from nanoplates and Janus particles at three ionic strengths (1.0, 1.4 and 1.6 mM). Scale bars: 5 μm. (B) The Janus particle coordination number distribution plots at different ionic strength conditions. In the horizontal coordinate, "0" means an unassembled Janus particle; "1" means a Janus particle with one chain attached; "2" means a Janus particle with two chains attached (highlighted by the orange circles in the optical microscopy image); ">2" means a Janus particle cluster. In all of these three plots, more than 120 Janus particles were measured and we compared regions where the chain−Janus particle concentration ratio is similar (0.7−0.8 on average) at the three ionic strength conditions. Note that the Janus particle coordination number distribution is slightly different at regions with different chain−Janus particle concentration ratios.

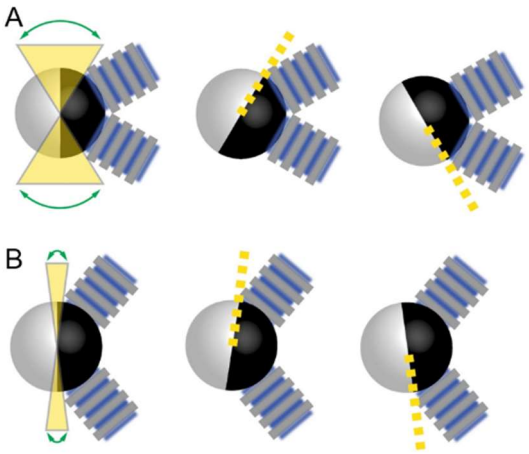

Figure S15. Schematics indicating the different degrees of Janus particle rotational entropy in the two-chain coordination case. (A) The case when the two chains on the Janus particle are in physical contact, giving the Janus particle more rotational entropy without reducing contact area with both chains on the Janus particle, as shown in the yellow region. (B) The case when the two chains on the Janus particle are away from each other, giving the Janus particle less rotational entropy, as shown in the yellow region.

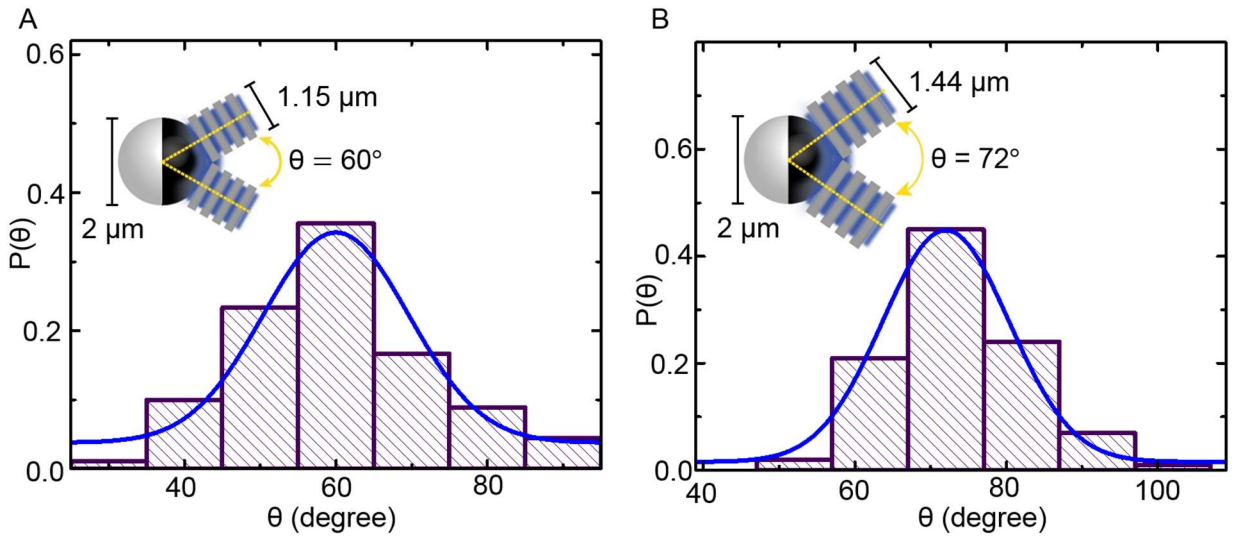

Figure S16. Experimental bond angle distributions in the two-chain coordination case with two different nanoplate−Janus particle size ratios at an ionic strength of 1.6 mM. (A) There is a dominant bond angle of 60° between the two silver chains (assembled from nanoplates with an average edge length of 1.15 μm) attached to the Janus particle (2 μm in diameter). (B) There is a dominant bond angle of 72° between the two silver chains (assembled from nanoplates with an average edge length of 1.44 μm) attached on the Janus particle (2 μm in diameter). In both cases, the bond angle distributions are obtained based on ~100 measurements. The dominant bond angle θ can be determined from the size ratio of Janus particles (diameter D) and chains (width W): $\theta = 2\tan^{-1}(W/D)$, as shown in Figure 5B.

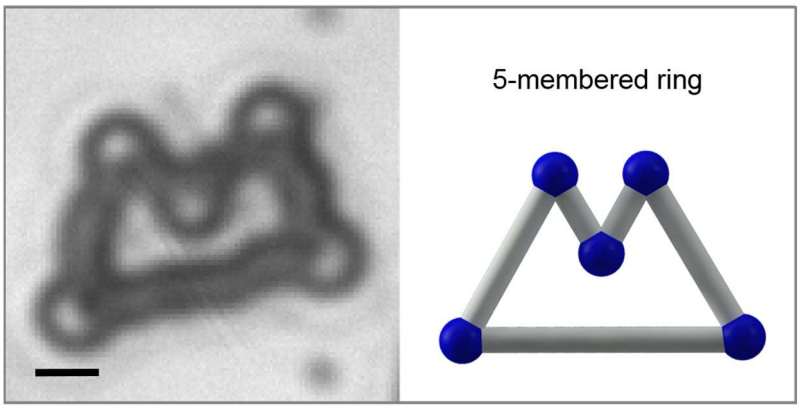

Figure S17. Optical microscopy image (left) of a 5-membered ring assembled from nanoplates with a 1.15 ± 0.14 μm edge length and Janus particles (2 μm in diameter). Ionic strength: 1.6 mM. Scale bar: 2 μm. The corresponding schematic (right) is drawn based on the color-coding used in Figure 5B.

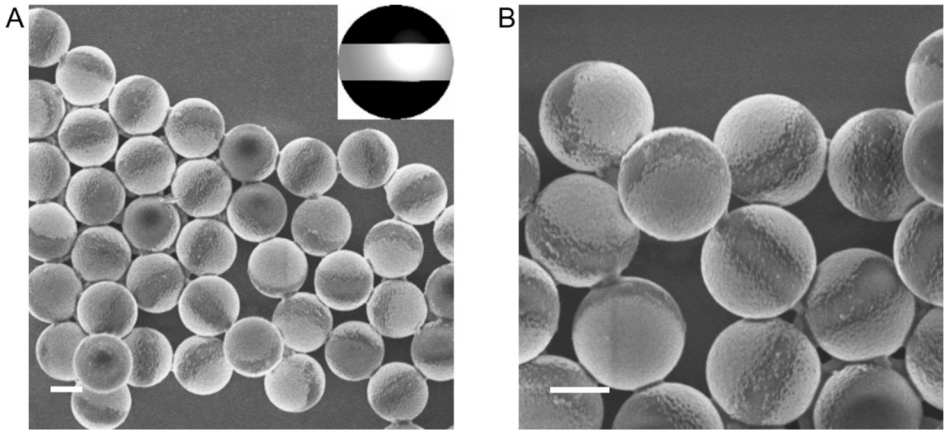

Figure S18. Low- (A) and high-magnification (B) SEM images of triblock particles with a diameter of 2 μm. The bright parts on the particle are the two gold patches and the dark part in the middle of the particle is the polystyrene side. The inset in (A) is a schematic of a triblock particle (gold in black, and polystyrene in white). Scale bars: 1 μm.

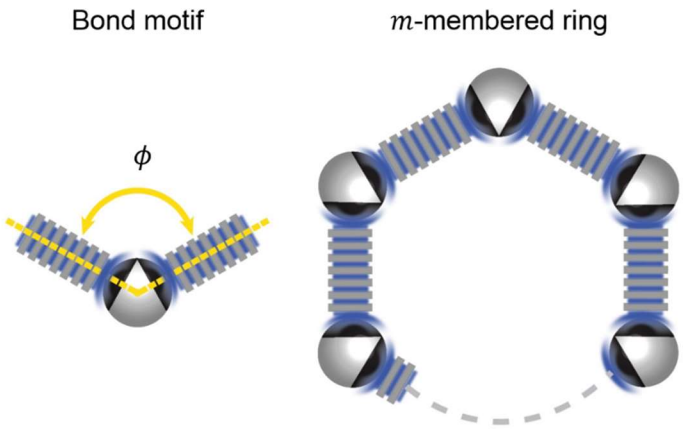

Figure S19. The m-membered ring structures one might expect from the co-assembly of angled patchy spheres and silver nanoplates. Here, m can be estimated by $m = \frac{360°}{180°-\phi}$, if the chain segments are of roughly uniform length and ϕ is the angle between the two gold patches on the polystyrene particle, which can be tuned following a reported method.[3]

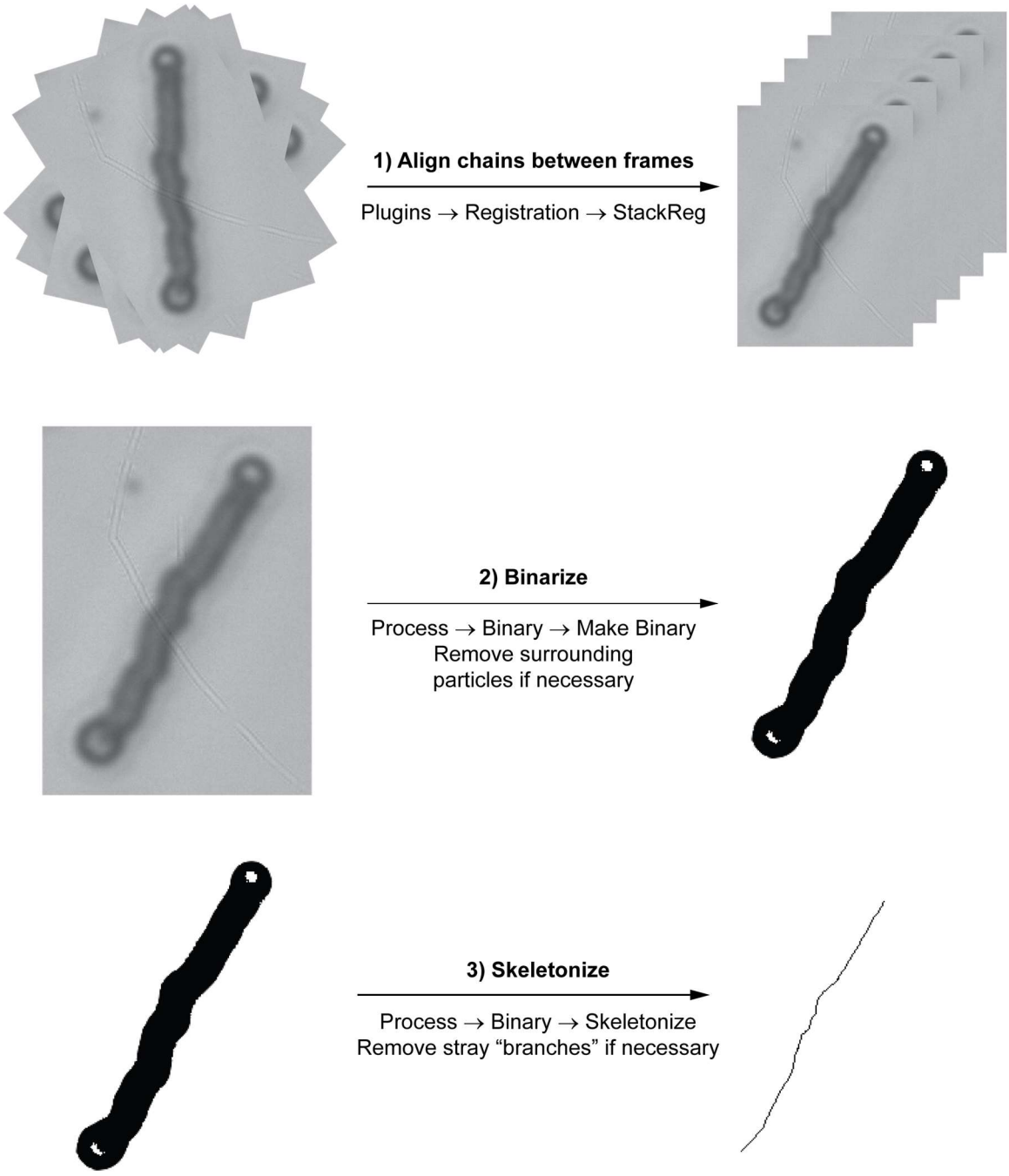

Figure S20. A detailed procedure showing the chain skeletonization process used in the chain fluctuation analysis. After aligning the chain between frames using the "rigid body" version of the "StackReg" function in ImageJ, images were binarized (Process → Binary → Make Binary) to generate a black and white image. We then used Process → Binary → Skeletonize to generate a single pixel-wide skeleton of the chain (only the silver chain segment, not including the Janus particles on chain ends). The pixel coordinates of this skeleton were used for later analysis.

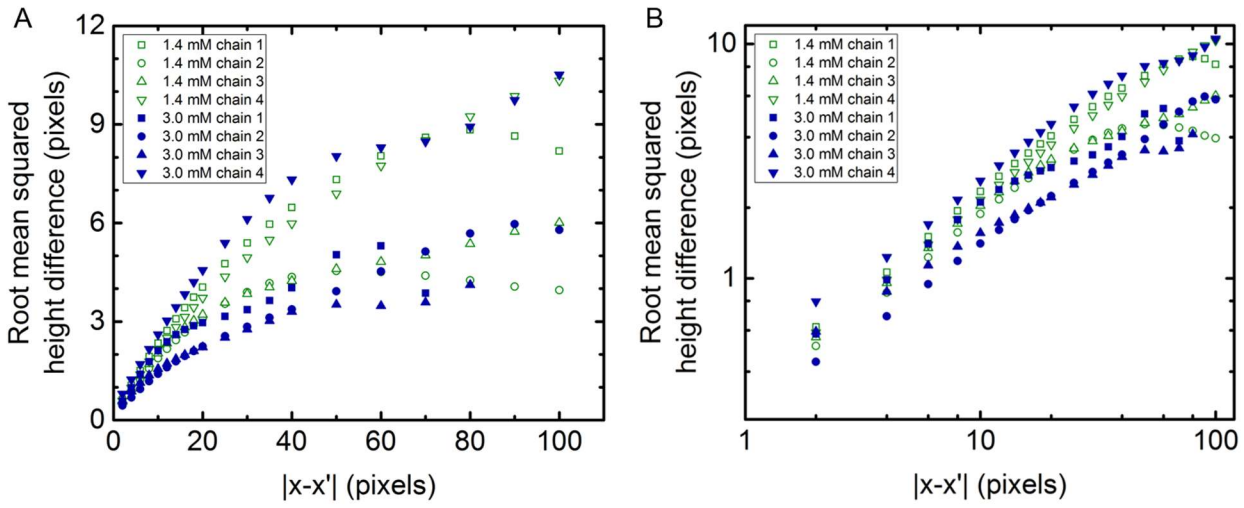

Figure S21. Root mean squared height difference (*i.e.*, $\langle (h(x) - h(x'))^2 \rangle^{1/2}$) as a function of chain coordinate separation $|x - x'|$ on linear (A) and log−log (B) plots for Janus particle-capped chains assembled in solutions with two different ionic strength conditions (1.4 and 3.0 mM). Pixel size: 1/73.86 nm. The four curves for each ionic strength condition were averaged to determine the curves displayed in Figure 4D. A power law fit to the linear portion of each curve defines a "roughness exponent" for a chain (See Table S4). These data come from analysis of 100 frames (about 5.81 s in total) for each chain.

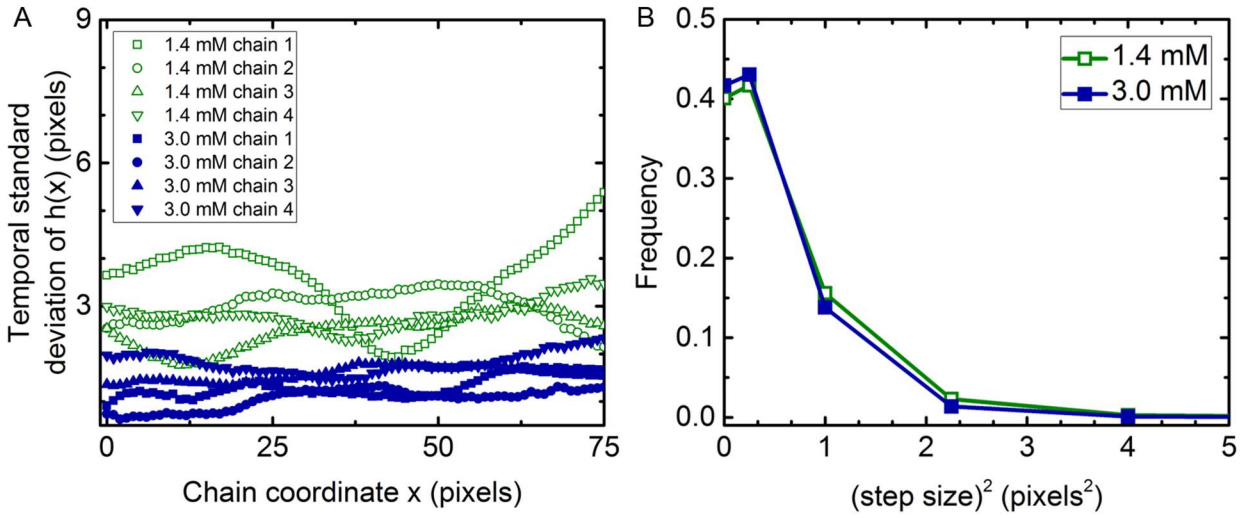

Figure S22. (A) An alternative characterization of the ionic strength-dependent fluctuations of chains. Each chain has a frame-specific height function $h(x,t)$ for which the height h at each particular point x fluctuates over t (in total 100 frames, or a span of ~5.81 s). Here are plotted the standard deviations of the height at each point x over this time span, *i.e.*, the standard deviation of $h(x,t)$ over t, for the eight different chains analyzed and for two ionic strengths conditions (1.4 and 3.0 mM). It is evident that the two ionic strengths are of distinct populations, with the heights at lower ionic strength varying more over time than those at higher ionic strength, when inter-nanoplate attractions are stronger (Figure S7). (B) Comparison of "step size" distributions at two different ionic strengths. This plot considers the frequencies of a particular squared step size between two points on a chain two pixels apart (*i.e.*, the distribution of $\big(h(x)-h(x+2)\big)^2$). These are the summed distributions for each of the eight chains analyzed (Figures 4D and S21). At 3.0 mM ionic strength, when attractions are stronger, chains have a higher frequency of smaller steps and a lower frequency of larger steps. At 1.4 mM ionic strength, chains have a higher frequency of larger steps and a lower frequency of smaller steps. Pixel size: 1/73.86 nm.

Tables S1−S6

Table S1. Synthesis conditions of silver nanoplates with different edge lengths.

Peak position of the seed solution (nm)	Peak intensity of the seed solution after dilution	Injection rate and time in each growth cycle	Shaking speed in growth cycle (rpm)	Growth cycle	Large nanoplate edge length (μm)	Related figure
705	0.012	0.4 mL/min, 5 min	300	Cycle 4	1.15 ± 0.14	5C
				Cycle 5	1.44 ± 0.26	2, 3, 4, 5A, S1
731	0.012	0.4 mL/min, 5 min	600	Cycle 3	1.09 ± 0.14	S2A
749	0.012	0.2 mL/min, 10 min	1000*	Cycle 4	1.46 ± 0.22	S2B
				Cycle 5	2.17 ± 0.33	S2C

*During the first cycle, a shaking speed of 700 rpm was used to prevent large-volume seed solution spilling out from the glass vial due to high-speed shaking.

Table S2. The calculated center-to-center d spacing values ($d = \frac{2\pi}{q_1}$) between neighboring nanoplates in the chain, peak positions q_1 to q_6, and ratios between higher-order peak positions (q_2 to q_6) and the first-order peak position q_1 in SAXS spectra at two different ionic strength conditions (1.4 and 3.0 mM). The first- or second-order peak was not shown in the measured range (see Figure 2B) and was derived based on higher-order peak positions.

Ionic strength (mM)	d (nm)	q_1 (1/Å)	q_2 (1/Å)	$\frac{q_2}{q_1}$	q_3 (1/Å)	$\frac{q_3}{q_1}$	q_4 (1/Å)	$\frac{q_4}{q_1}$	q_5 (1/Å)	$\frac{q_5}{q_1}$	q_6 (1/Å)	$\frac{q_6}{q_1}$
1.4	116.6	0.00539*	0.0108*	2.0	0.0161	3.0	0.0216	4.0	0.0270	5.0	0.0334	6.2
3.0	85.5	0.00735*	0.0147	2.0	0.0222	3.0	0.0299	4.1	0.0376	5.1	0.0451	6.1

*These q values were derived based on higher-order peak positions.

Table S3. Comparison of the number-average degrees of polymerization $\bar{X}_{\mathrm{n}}$ obtained from "chain stopper" model ($\bar{X}_{\mathrm{n}} = 2/(2(1-p) + \frac{c_{\mathrm{s}}}{c_{\mathrm{m}}} p e^{-|\Delta U|/k_{\mathrm{B}}T})$) and experimental results. The errors are from measurement errors. Here, p is the extent of reaction of nanoplates obtained from Flory−Schulz distribution fitting for i-mer fraction distribution (Figure 3B), c_{s} is the Janus particle concentration, and c_{m} is the nanoplate concentration, ΔU is the difference between nanoplate−nanoplate and nanoplate−Janus particle interaction strengths at an ionic strength of 1.4 mM used in this experiment.

$\frac{c_{\mathrm{s}}}{c_{\mathrm{m}}}$ (from experiment)	p (from fitting)	$\bar{X}_{\mathrm{n}}$ (from experiment)	$\bar{X}_{\mathrm{n}}$ (from fitting)
0%	0.9931	143 ± 8	145
1.2%	0.9900	90 ± 6	92
3.5%	0.9792	47 ± 6	43

Table S4. Roughness exponents and persistence length values for each of the eight chains analyzed. The roughness exponent values were determined by fitting the linear regimes (to a point where a linear fit had an R^2 value of at least 0.98) of log−log plots shown in Figure S21B. The errors shown in the averaged values for both ionic strength conditions are the standard deviation among different chains. The errors in the persistence length for each chain are from averaging persistence lengths for different modes.

Ionic strength	Chain labeling (length)	Roughness exponent α	Persistence length (μm)
1.4 mM	chain 1 (13.96 μm)	0.753	103 ± 31
	chain 2 (10.34 μm)	0.730	119 ± 28
	chain 3 (13.00 μm)	0.730	105 ± 26
	chain 4 (20.39 μm)	0.735	112 ± 44
1.4 mM average		0.737 ± 0.011	
3.0 mM	chain 1 (5.69 μm)	0.750	178 ± 37
	chain 2 (9.53 μm)	0.673	271 ± 158
	chain 3 (6.57 μm)	0.559	181 ± 88
	chain 4 (13.74 μm)	0.735	292 ± 155
3.0 mM average		0.679 ± 0.087	

Table S5. Comparison between the relative contraction of co-assembled chains upon an ionic strength increase from 1.4 mM to 3.0 mM as obtained from optical microscopy (Movie S5 and Figure 4C), SAXS, and theoretical calculations. The chain length measurements from optical microscopy images are based on measuring length of the nanoplate portion of co-assembled chain before and after contraction, not including the Janus particles capped on the chain ends. The errors shown in chain length measurements are from measurement errors. The errors shown in SAXS data are from averaging three SAXS measurements at each ionic strength condition.

	1.4 mM	3.0 mM	Relative contraction
Length of chain 1 (μm)	28.05 ± 1.40	18.74 ± 0.94	0.67 ± 0.07
Length of chain 2 (μm)	21.79 ± 1.09	15.31 ± 0.77	0.71 ± 0.07
Length of chain 3 (μm)	20.51 ± 1.03	14.81 ± 0.74	0.73 ± 0.08
Averaging three chains			0.70 ± 0.08
d from SAXS (nm)	116.9 ± 0.3	85.1 ± 0.9	0.73 ± 0.01
d from calculation (nm)	100.0	73.6	0.74

Table S6. The parameters used in the nanoplate−nanoplate interaction calculation.

Interaction	Parameter	Value
van der Waals attraction	Hamaker constant (H)	1.6×10^{-19} J
	nanoplate edge length (a)	1.44 μm
	nanoplate thickness (t_{plate})	29 nm
electrostatic repulsion	carboxylate−thiol ligand monolayer thickness (t_{ligand})	2.4 nm
	relative permittivity of water (ε)	78.5
	vacuum permittivity (ε_0)	8.854×10^{-12} F/m
	zeta potential of silver nanoplates (ζ)	−41.9 mV

Movies S1−S8

Movie S1. An optical microscopy movie showing chain growth by both "monomer" addition and the fusion of shorter chains. Ionic strength: 1.4 mM. The real time rounded to the nearest whole second is shown in the time stamp. The movie is played at 17.21 fps at 1x speed. Scale bar: 6 μm.

Movie S2. An optical microscopy movie showing the disassembly behavior of assembled chains upon a decrease in ionic strength from 1.4 mM to 0.5 mM, by carefully adding water to the system. The directional diffusion was caused by the addition of water. The real time rounded to the nearest whole second is shown in the time stamp. The movie is played at 8.6 fps (using every twentieth frame of a 17.21 fps movie recorded) at 10x speed. Scale bar: 6 μm.

Movie S3. An optical microscopy movie showing chains assembled from very large nanoplate with an average edge length of 2.17 μm. Ionic strength: 0.9 mM. The real time rounded to the nearest whole second is shown in the time stamp. The movie is played at 20 fps at 1x speed. Scale bar: 6 μm.

Movie S4. Two optical microscopy movies showing the same fluctuating co-assembled chain at two different ionic strength conditions (top: 1.4 mM; bottom: 3.0 mM) and the corresponding synchronized plots showing the fluctuations of the chain skeleton over time. This is the same chain tracked in Movie S5. The skeleton is color-coded according to the extent of transverse displacement. The unit of the color bar is the pixel size (1/73.86 nm). The movie is played at 6.9 fps (using every tenth frame of a 17.21 fps movie recorded) at 4x speed. Scale bars: 4 μm.

Movie S5. An optical microscopy movie (left) showing the contraction of a chain capped with Janus particles upon increasing the ionic strength from 1.4 mM to 3.0 mM and a synchronized plot (right) showing the corresponding length of the nanoplate portion of the chain as a function as time. The increase in ionic strength was performed by adding NaCl solution to the system through a syringe pump with an injection rate of 0.08 mL/min. This is the same chain analyzed in Movie S4. The real time rounded to the nearest whole second is shown in the time stamp. The movie is played at 13.8 fps (using every tenth frame of a 17.21 fps movie recorded) at 8x speed. Scale bar: 4 μm.

Movie S6. An optical microscopy movie (left) showing the closing of a triangular ring and a synchronized plot (right) showing the corresponding bond angle (θ) fluctuation as a function of time. The bond angle before ring closure displays ample fluctuations around 60° but afterwards stays closer to 60° (in the region

marked by the green lines) to minimize the strain inside the triangular ring. The real time rounded to the nearest whole second is shown in the time stamp. Ionic strength: 1.6 mM. The movie is played at 9 fps (using every second frame of an 18 fps movie recorded) at 1x speed. Scale bar: 2 μm.

Movie S7. An optical microscopy movie (left) showing the contraction of a triangular ring upon increasing the ionic strength from 1.6 mM to 3.0 mM and a plot (right) showing the area of the pore in the triangular ring as a function as time. The increase in ionic strength was performed by adding NaCl solution to the system through a syringe pump with an injection rate of 0.03 mL/min. The real time rounded to the nearest whole second is shown in the time stamp. The movie is played at 8.6 fps (using every twentieth frame of a 17.21 fps movie recorded) at 10x speed. Scale bar: 2 μm.

Movie S8. A fluorescence microscopy together with bright-field optical microscopy movie showing the "zigzag" structure co-assembled from nanoplates and Janus particles. The real time rounded to the nearest whole second is shown in the time stamp. The movie is played at 20 fps at 1x speed. Scale bar: 3 μm.

References

(1) Zhang, Q.; Hu, Y.; Guo, S.; Goebl, J.; Yin, Y. Seeded Growth of Uniform Ag Nanoplates with High Aspect Ratio and Widely Tunable Surface Plasmon Bands. *Nano Lett.* **2010**, *10*, 5037-5042.

(2) Chen, Q.; Whitmer, J. K.; Jiang, S.; Bae, S. C.; Luijten, E.; Granick, S. Supracolloidal Reaction Kinetics of Janus Spheres. *Science* **2011**, *331*, 199-202.

(3) Chen, Q.; Diesel, E.; Whitmer, J. K.; Bae, S. C.; Luijten, E.; Granick, S. Triblock Colloids for Directed Self-Assembly. *J. Am. Chem. Soc.* **2011**, *133*, 7725-7727.

(4) Schnablegger, H.; Singh, Y. *The SAXS Guide,* 3rd ed.; Anton Paar GmbH, 2013; pp 25-26.

(5) Flory, P. J. *Principles of Polymer Chemistry*; Cornell Univ. Press, New York, 1953.

(6) Odian, G. *Principles of Polymerization,* 4th ed.; Wiley, New York, 2004.

(7) Liu, K.; Nie, Z.; Zhao, N.; Li, W.; Rubinstein, M.; Kumacheva, E. Step-Growth Polymerization of Inorganic Nanoparticles. *Science* **2010**, *329*, 197-200.

(8) Rubenstein, M.; Colby, R. H. *Polymer Physics*; Oxford Univ. Press, Oxford, 2003.

(9) Young, K. L.; Jones, M. R.; Zhang, J.; Macfarlane, R. J.; Esquivel-Sirvent, R.; Nap, R. J.; Wu, J.; Schatz, G. C.; Lee, B.; Mirkin, C. A. Assembly of Reconfigurable One-Dimensional Colloidal Superlattices due to a Synergy of Fundamental Nanoscale Forces. *Proc. Natl. Acad. Sci. U. S. A.* **2012**, *109*, 2240-2245.

(10) Walker, D. A.; Browne, K. P.; Kowalczyk, B.; Grzybowski, B. A. Self-Assembly of Nanotriangle Superlattices Facilitated by Repulsive Electrostatic Interactions. *Angew. Chem., Int. Ed.* **2010**, *49*, 6760-6763.

(11) Skoglund, S.; Lowe, T. A.; Hedberg, J.; Blomberg, E.; Wallinder, I. O.; Wold, S.; Lundin, M. Effect of Laundry Surfactants on Surface Charge and Colloidal Stability of Silver Nanoparticles. *Langmuir* **2013**, *29*, 8882-8891.

(12) Kim, J.; Jones, M. R.; Ou, Z.; Chen, Q. *In Situ* Electron Microscopy Imaging and Quantitative Structural Modulation of Nanoparticle Superlattices. *ACS Nano* **2016**, *10*, 9801-9808.

(13) Jones, M. R.; Macfarlane, R. J.; Prigodich, A. E.; Patel, P. C.; Mirkin, C. A. Nanoparticle Shape Anisotropy Dictates the Collective Behavior of Surface-Bound Ligands. *J. Am. Chem. Soc.* **2011**, *133*, 18865-18869.

(14) Bishop, K. J. M.; Wilmer, C. E.; Soh, S.; Grzybowski, B. A. Nanoscale Forces and Their Uses in Self-Assembly. *Small* **2009**, *5*, 1600-1630.

(15) Li, D.; Banon, S.; Biswal, S. L. Bending Dynamics of DNA-Linked Colloidal Particle Chains. *Soft Matter* **2010**, *6*, 4197-4204.

(16) Brangwynne, C. P.; Koenderink, G. H.; Barry, E.; Dogic, Z.; MacKintosh, F. C.; Weitz, D. A. Bending Dynamics of Fluctuating Biopolymers Probed by Automated High-Resolution Filament Tracking. *Biophys. J.* **2007**, *93*, 346-359.

(17) Käs, J.; Strey, H.; Tang, J. X.; Finger, D.; Ezzell, R.; Sackmann, E.; Janmey, P. A. F-Actin, a Model Polymer for Semiflexible Chains in Dilute, Semidilute, and Liquid Crystalline Solutions. *Biophys. J.* **1996**, *70*, 609-625.

(18) Domínguez-García, P.; Melle, S.; Rubio, M. A. Morphology of Anisotropic Chains in a Magneto-Rheological Fluid during Aggregation and Disaggregation Processes. *J. Colloid Interface Sci.* **2009**, *333*, 221-229.

(19) Furst, E. M.; Gast, A. P. Dynamics and Lateral Interactions of Dipolar Chains. *Phys. Rev. E* **2000**, *62*, 6916-6925.

(20) Silva, A. S.; Bond, R.; Plouraboué, F.; Wirtz, D. Fluctuation Dynamics of a Single Magnetic Chain. *Phys. Rev. E* **1996**, *54*, 5502-5510.

(21) Yang, H. N.; Lu, T. M. Inconsistency between Height-Height Correlation and Power-Spectrum Functions of Scale-Invariant Surfaces for Roughness Exponent $\alpha \sim 1$. *Phys. Rev. B* **1995**, *51*, 2479-2483.

(22) Buceta, J.; Pastor, J.; Rubio, M. A.; de la Rubia, F. J. Finite Resolution Effects in the Analysis of the Scaling Behavior of Rough Surfaces. *Phys. Rev. E* **2000**, *61*, 6015-6018.

(23) Gittes, F.; Mickey, B.; Nettleton, J.; Howard, J. Flexural Rigidity of Microtubules and Actin Filaments Measured from Thermal Fluctuations in Shape. *J. Cell Biol.* **1993**, *120*, 923-934.

(24) Usov, I.; Mezzenga, R. FiberApp: An Open-Source Software for Tracking and Analyzing Polymers, Filaments, Biomacromolecules, and Fibrous Objects. *Macromolecules* **2015**, *48*, 1269-1280.

(25) Tigges, T.; Walther, A. Hierarchical Self-Assembly of 3D-Printed Lock-and-Key Colloids through Shape Recognition. *Angew. Chem., Int. Ed.* **2016**, *55*, 11261-11265.